

Hosts and triggers of AGNs in the Local Universe

Ziwen Zhang^{1,2}, Huiyuan Wang^{1,2}, Wentao Luo^{3,1}, H.J. Mo⁴, Zhixiong Liang^{1,2}, Ran Li^{5,6}, Xiaohu Yang⁷,
Tinggui Wang^{1,2}, Hongxin Zhang^{1,2}, Hui Hong^{1,2}, Xiaoyu Wang^{1,2}, Enci Wang⁸, Pengfei Li^{1,2} and JingJing
Shi³

¹ CAS Key Laboratory for Research in Galaxies and Cosmology, Department of Astronomy, University of Science and Technology of China, Hefei, Anhui 230026, China; Email: ziwen@mail.ustc.edu.cn, whywang@ustc.edu.cn

² School of Astronomy and Space Science, University of Science and Technology of China, Hefei 230026, China

³ Institute for the Physics and Mathematics of the Universe (Kavli IPMU, WPI), UTIAS, Tokyo Institutes for Advanced Study, University of Tokyo, Chiba, 277-8583, Japan

⁴ Department of Astronomy, University of Massachusetts, Amherst MA 01003-9305, USA

⁵ Key laboratory for Computational Astrophysics, National Astronomical Observatories, Chinese Academy of Sciences, Beijing 100012, China

⁶ College of Astronomy and Space Sciences, University of Chinese Academy of Sciences, 19A Yuquan Road, Beijing 100049, China

⁷ Department of Astronomy, and Tsung-Dao Lee Institute, Shanghai Jiao Tong University, Shanghai 200240, China

⁸ Department of Physics, ETH Zurich, Wolfgang-Pauli-Strasse 27, CH-8093 Zurich, Switzerland

May 3, 2021

ABSTRACT

Based on the spectroscopic and shear catalogs for SDSS galaxies in the local Universe, we compare optically-selected active galactic nuclei (AGNs) with control star-forming and quiescent galaxies on galactic, inter-halo and larger scales. We find that AGNs are preferentially found in two specific stages of galaxy evolution: star-burst and ‘green valley’ phases, and that the stellar population of their host galaxies is quite independent of stellar mass, different from normal galaxies. Combining galaxy-galaxy lensing and galaxy clustering on large scales, we measure the mass of AGN host halos. The typical halo mass is about $10^{12} h^{-1} M_{\odot}$, similar to the characteristic mass in the stellar mass-halo mass relation (SHMR). For given stellar mass, AGN host galaxies and star-forming galaxies share the same SHMR, while quiescent galaxies have more massive halos. Clustering analysis on halo scales reveals that AGNs are surrounded by a larger number of satellites (with stellar mass down to 1/1000 of the mass of the central galaxy) than star-forming galaxies, and that galaxies with larger stellar velocity dispersion have more satellites. The number of satellites also increase with halo mass, reaching unity around $10^{12} h^{-1} M_{\odot}$. Our results suggest a scenario, in which the interaction of the central galaxy with the satellites triggers an early episode of star burst and AGN activities, followed by multiple AGN cycles driven by the non-axisymmetric structure produced by the interaction. The feedback from the starburst and AGN reduces the amount of cold gas for fueling the central black hole, producing a characteristic halo mass scale, $\sim 10^{12} h^{-1} M_{\odot}$, where the AGN fraction peaks.

Key words. gravitational lensing: weak - galaxies: halos - galaxies: general - galaxies: Seyfert - methods: statistical

1. Introduction

In the local Universe, galaxies can be divided into two distinct populations: quiescent and star-forming galaxies (e.g. Strateva et al. 2001; Baldry et al. 2004; Brinchmann et al. 2004; Wetzel et al. 2012). The number density of quiescent galaxies continuously increases with cosmic time since redshift of about four (e.g. Bell et al. 2004; Ilbert et al. 2013; Muzzin et al. 2013; Tomczak et al. 2014; Barro et al. 2017), suggesting that galaxy quenching is an important process that drives galaxy evolution over most of the Hubble time. To understand the underlying mechanisms, extensive studies have been carried out to search for the correlation of galaxy quenching with both internal properties of galaxies and their environments (e.g. Baldry et al. 2006; Weinmann et al. 2006; van den Bosch et al. 2008; Peng et al. 2010; Wetzel et al. 2012; Woo et al. 2013; Bluck et al. 2014; Wang et al. 2016, 2018b,a; Bluck et al. 2020; Li et al. 2020).

For central galaxies, which are the dominant galaxies in dark matter halos, the most important internal and environmental parameters seem to be the central velocity dispersion of the galaxy and the halo mass respectively (Bluck et al. 2020). This indicates that mechanisms that are related to the galaxy bulge mass or central black hole mass, such as the active galactic nuclei (AGN) feedback (Silk & Rees 1998; Croton et al. 2006; Heckman & Best 2014), and those related to halo mass, such as galaxy interaction (e.g. Moore et al. 1996; Conselice et al. 2003; Di Matteo et al. 2005) and virial shock heating (e.g. Dekel & Birnboim 2006; Gabor & Davé 2015), may be responsible for the quenching. These mechanisms, in particular the AGN feedback, are expected to become dominant for massive galaxies, and help to yield a ‘pivot halo mass’, $M_{h,p} \sim 10^{12} h^{-1} M_{\odot}$, in the stellar mass-halo mass relation (SHMR), at which, the efficiency for galaxy formation is maximum (e.g. Yang et al. 2003; Wechsler & Tinker 2018).

However the observational evidence for AGN feedback remains elusive. Indeed, AGN feedback has been reported to both enhance and suppress star formation (e.g. Fabian 2012; Mullaney et al. 2015; Delvecchio et al. 2015; Rodighiero et al. 2015; Kalfountzou et al. 2017; Mahoro et al. 2017; Bing et al. 2019). One important reason for this uncertainty is that the lifetime of AGN activities, which is about 10^5 to 10^8 years (e.g. Marconi et al. 2004; Schawinski et al. 2015; Yuan et al. 2018), is much shorter than the quenching time scale (typically about 1 Gyrs, Bell et al. 2004; Blanton 2006), so that it is difficult to find an instantaneous correlation between AGN and star formation activities directly from observational data.

The locus of AGNs in the evolutionary path from star-forming galaxies to quiescent galaxies may provide valuable information about the role of AGNs. Previous studies have revealed some interesting trends. For example, some studies found that the host galaxies of AGNs appear to be located at the green valley, which is the transition region from star-forming to quiescent galaxies (Heckman & Best 2014; Man et al. 2019; Dodd et al. 2020). Moreover, studies based on AGN clustering, weak lensing and galaxy groups all suggests that optically selected AGNs at low redshift reside preferentially in halos of roughly $M_{h,A} = 10^{12} h^{-1} M_{\odot}$ (e.g. Croom et al. 2005; Pasquali et al. 2009; Mandelbaum et al. 2009; Shen et al. 2013), similar to the pivot halo mass, suggesting that optical AGNs may be at a special stage of galaxy evolution. It is thus interesting to understand why optical AGNs favor halos of $M_{h,A} = 10^{12} h^{-1} M_{\odot}$ and what processes, in these halos are responsible for triggering AGN activities.

Many factors can affect the prevalence of AGN activities. One important question is how to bring the gas down to the galaxy center to fuel the supermassive black holes (SMBH). In the literature, two kinds of mechanisms are proposed. One is the internal secular evolution process. The torque induced by non-axisymmetric galactic structures can drive slow and significant inflow (Kormendy & Kennicutt 2004; Hopkins & Quataert 2011; Sellwood 2014; Fanali et al. 2015). The galactic bar is one of the most prominent non-axisymmetric structures, and exists in about 40% of spiral galaxies (Oh et al. 2012). And there is evidence showing that bars can enhance star formation in the central regions of galaxies (e.g. Oh et al. 2012; Chown et al. 2019). However, whether galactic bars can significantly affect AGN activity is still under debate (Arsenault 1989; Mulchaey & Regan 1997; Oh et al. 2012; Galloway et al. 2015; Goulding et al. 2017; Alonso et al. 2018).

Other mechanisms, such as galaxy merger and interaction, are also expected to displace the angular momentum of the gas and transport the gas inward (e.g. Hopkins et al. 2006; Di Matteo et al. 2008; Bhowmick et al. 2020). Similar to the studies of secular evolution, observational evidence for this scenario is also mixed. Some studies found significant environmental dependence of AGN activities (e.g. Koulouridis et al. 2006; Koss et al. 2010; Ellison et al. 2011; Sabater et al. 2013; Khabiboulline et al. 2014; Lackner et al. 2014; Satyapal et al. 2014; Hong et al. 2015; Kocevski et al. 2015; Goulding et al. 2018; Gao et al. 2020), while others found no or only weak environmental effects (e.g. Grogin et al. 2005; Li et al. 2006b; Pierce et al. 2007; Ellison et al. 2008; Li et al. 2008; Gabor et al. 2009; Darg et al. 2010; Wang & Li 2019; Man et al. 2019). The contradictory results may be caused by the difference in AGN

selection criterion, observational bias, control sample and environmental indicator used. As we will show below, understanding environmental effects on AGNs also requires the knowledge about the evolutionary status of their host galaxies, as it can help us to better understand how to construct control samples and to adopt appropriate environmental indicators.

In this paper, we combine galaxy-galaxy weak lensing and galaxy clustering measurement to constrain the host halo masses of optically selected AGNs and their control samples. To take into account the galaxy evolution, we split the control sample into star-forming and quiescent galaxies. We compare internal properties, small-scale clustering and halo mass of galaxies in the three samples to put AGNs in the evolutionary track of galaxy evolution and to understand the role of environmental processes.

The paper is organized as follows. Section 2 presents the AGN sample selection, control sample construction, and the methods of using galaxy clustering and galaxy-galaxy (g-g) lensing to derive halo mass. In Section 3, we compare the properties of AGN host galaxies with those of control samples. In Section 4, we use g-g lensing and galaxy clustering to measure the mass of AGN host halos in comparison to that of the control samples. In Section 5, we analyze satellites around AGNs and normal samples. We discuss the importance of using well-defined control samples, environmental triggering of AGN activities, and the connection of AGN feedback and galaxy evolution in Section 6. Finally, we summarize our results in Section 7.

2. Samples and Methods of Analysis

2.1. AGN samples and control samples of normal galaxies

Our galaxy sample is drawn from the New York University Value Added Galaxy Catalog (NYU-VAGC) sample (Blanton et al. 2005) of the Sloan Digital Sky Survey (SDSS) DR7 (Abazajian et al. 2009). In this paper, we mainly focus on central galaxies, which is defined as the most massive galaxies in galaxy groups. Here, we use the galaxy group catalog constructed by using the halo-based group-finding algorithm (Yang et al. 2005, 2007) to separate centrals from satellites. Following Yang et al. (2007), we select galaxies with r-band Petrosian magnitudes $r \leq 17.72$, with redshifts in the range $0.01 \leq z \leq 0.2$, and with redshift completeness $C_z > 0.7$. Stellar mass of individual galaxies, M_* , are obtained using the relation between the stellar mass-to-light ratio and color, as given by Bell et al. (2003), but assuming a Kroupa IMF (Kroupa 2001). This leads to a -0.1 dex correction in the stellar mass-to-light ratios relative to the original values. To obtain the star formation rate (SFR) and 4000Å break (D_n4000) of individual galaxies, we combine our galaxy sample with the MPA/JHU SDSS catalog (Brinchmann et al. 2004). The total galaxy sample (tG) contains 593,227 galaxies, of which 452,177 are identified as centrals (hereafter cG).

Active galactic nuclei (AGNs) are identified using the BPT diagram (Baldwin et al. 1981) from the tG sample. In particular, we use the demarcation line proposed by Kauffmann et al. (2003a), in the [OIII] λ 5007/H β versus [NII] λ 6583/H α diagram. The fluxes of the four emission lines are taken from the MPA/JHU catalog. Following Brinchmann et al. (2004), we require the four spectral lines to have a signal-to-noise ratio greater than 3.0. These se-

lection criteria result in a total of 57,252 AGNs (hereafter tAGN sample). Among them, 46,198 are central galaxies, and the corresponding sample is denoted by cAGN.

A control sample of galaxies is constructed by simultaneously matching both the redshift and the stellar mass (M_*). The adopted tolerances in the matching are $|\Delta z| < 0.005$ and $|\Delta \log_{10} M_*| < 0.1$. For each AGN, four control galaxies are selected. Several types of control samples are constructed. For the tAGN sample, we construct a control sample, tG^c, from the tG sample. For the cAGN sample, a control sample, cG^c, is constructed from the cG sample. We also separate galaxies into a star-forming population and a quiescent population in the SFR- M_* space, using the demarcation line proposed by Bluck et al. (2016). Thus, for the cAGN sample, we also construct a control star-forming (cSF^c) sample and a control quiescent (cQ^c) sample.

As shown below, the stellar velocity dispersion (σ_*) for AGNs is systematically different from other galaxies of the same stellar mass. We thus also construct control samples according to σ_* . The values of σ_* are also taken from the NYU-VAGC and corrected to the same effective aperture using the formula of Cappellari et al. (2006). The control samples, cSF^{c σ_*} and cQ^{c σ_*} , are constructed, respectively, from the star-forming and quiescent galaxies with σ_* measurements, by matching redshift, M_* and σ_* . The tolerance in σ_* is $|\Delta \sigma_*| < 20 \text{ km s}^{-1}$. Some AGNs have no σ_* measurements and/or no matched galaxies. Excluding these galaxies results in 43,851 central AGNs, and this new AGN sample is referred to as cAGN $_{\sigma_*}$. For comparison, we also construct another set of control samples, cSF^{c σ_*} and cQ^{c σ_*} , for cAGN $_{\sigma_*}$, by only matching stellar mass and redshift.

The first lowercase letter, ‘t’ or ‘c’, in the sample name indicates that the sample includes both centrals and satellites (total) or only centrals. The superscript, ‘c’, indicates the control samples with stellar mass and redshift controlled, while ‘c2’ indicates the control samples with σ_* additionally controlled. If a sample has no superscript, it is not a control sample, such as cAGN and cG. Most of our following analyses focus on the cAGN sample and its control samples.

2.2. The cross-correlation analysis

The auto-correlation functions of AGNs and the AGN-galaxy cross correlation function provide effective ways to study the large scale environments of AGNs (e.g. Croom et al. 2005; Li et al. 2006b; Shen et al. 2013; Zhang et al. 2013; Jiang et al. 2016; Laurent et al. 2017; Shankar et al. 2019). Here we use the projected two-point cross-correlation function (hereafter 2PCCF) to quantify the clustering of our selected sample with respect to the corresponding reference galaxy sample. The reference sample is constructed in exactly the same way as described in Wang & Li (2019), and here we provide a brief description about the construction. The reference sample is a magnitude-limited sample selected from the NYU-VAGC sample (Blanton et al. 2005). It consists of 510,605 galaxies with r -band Petrosian apparent magnitude of $r < 17.6$, with $-24 < M_{0.1r} < -16$, and with spectroscopic redshift in range $0.01 < z < 0.2$. Here, $M_{0.1r}$ is the r -band Petrosian absolute magnitude, $K + E$ -corrected to $z = 0.1$. The random sample is constructed following the method described in Li et al. (2006a). For each galaxy in the reference sample, we duplicate it at 10 randomly-selected sky positions in the SDSS survey

area,¹ keeping all other properties (including redshift) of the galaxy unchanged. The resulted random sample has the same survey geometry, the same distribution of galaxy intrinsic properties, and the same redshift distribution as the reference sample. The 2PCCF is statistically more robust than the auto-correlation function, because we can use the large number of reference galaxies to determine both the small and large scale environments of AGNs. The 2PCCF on small scales describes the abundance of neighboring galaxies around the selected galaxies, and that on large scales carries information about halo bias, thereby providing constraints on the host halo mass of AGNs (e.g. Mo & White 1996).

We estimate the 2PCCF, $\xi(r_p, \pi)$, using

$$\xi(r_p, \pi) = \frac{N_R}{N_D} \frac{GD(r_p, \pi)}{GR(r_p, \pi)} - 1, \quad (1)$$

where N_D and N_R are the galaxy numbers in the reference and random samples, respectively; r_p and π are the separations perpendicular and parallel to the line of sight, respectively; GD is the number of cross pairs between the selected sample and the reference sample; GR is that between the selected sample and the random sample.

Integrating $\xi(r_p, \pi)$ along the line of sight to reduce the redshift distortion effect, we obtain the projected 2PCCF,

$$w_p(r_p) = 2 \int_0^\infty \xi(r_p, \pi) d\pi = 2 \sum_i \xi(r_p, \pi_i) \Delta \pi_i, \quad (2)$$

where π_i and $\Delta \pi_i$ are the separation parallel to the line of sight and the corresponding bin size. We adopt $\pi_{\max} = 40 \text{ h}^{-1} \text{ Mpc}$ as the upper limit of the integration and $\Delta \pi_i = 1 \text{ h}^{-1} \text{ Mpc}$. We sample r_p in 10 logarithmic bins with $r_{p,\min} = 0.01 \text{ h}^{-1} \text{ Mpc}$ and $\Delta \log(r_p / \text{h}^{-1} \text{ Mpc}) = 0.345$. The errors on the measurements of the 2PCCF are estimated by using 100 bootstrap samples (Barrow et al. 1984). We correct the fiber collision effects by using the same method as in Li et al. (2006a), and we refer the reader to the original paper for details and validity tests.

2.3. Weak-lensing shear measurements and halo-mass estimates

The shear catalog used here is created by Luo et al. (2017). Their selection of source galaxies is from SDSS DR7 image data in the r band, which covers about 8423 square degrees of the SDSS LEGACY sky. A sequence of Flags and model magnitude cuts with $r \leq 22.0$ and $i \leq 21.5$ are applied to the image data. The shapes of the galaxy images are obtained, and the final shape catalog consists of the shape measurements with the resolution factor R equal or greater than 1/3. This shape catalog contains 39,625,244 galaxies with positions, shapes, and photo- z information for individual source galaxies.

We measure the galaxy-galaxy lensing signal by stacking the tangential ellipticity of source galaxies in projected radial bins (Miralda-Escude 1991; Sheldon et al. 2004; Mandelbaum et al. 2005, 2009; Luo et al. 2018). The non-zero

¹ The geometry of the survey area is described by a set of spherical polygons, see <http://sdss.physics.nyu.edu/vagc/> (Blanton et al. 2005).

tangential ellipticity, a.k.a the tangential shear (γ_t) is related to the excess surface density (ESD), $\Delta\Sigma$, by

$$\Delta\Sigma(r_p) = \gamma_t \Sigma_{\text{crit}} = \bar{\Sigma}(< r_p) - \Sigma(r_p), \quad (3)$$

where $\bar{\Sigma}(< r_p)$ is the average surface mass density within r_p , $\Sigma(r_p)$ is the surface mass density at r_p , and Σ_{crit} is the geometrical factor defined as

$$\Sigma_{\text{crit}} = \frac{c^2}{4\pi G} \frac{D_s}{D_1 D_{1s} (1 + z_l)^2}, \quad (4)$$

where c is the speed of light, G is the gravity constant, z_l is the redshift of the lens, D_{1s} is the angular diameter distance between the lens and the source, D_1 and D_s are the angular diameter distances of the lens and the source, respectively. In addition, we estimate the errors of the lensing signal by using 2,500 bootstrap samples.

We use two models to fit the weak lensing signal around galaxies. The first one (hereafter M1) assumes that the lensing signal as the combination of three terms,

$$\Delta\Sigma(r_p) = \Delta\Sigma_{\text{NFW}}^{\text{off}}(r_p) + \frac{M_*}{\pi r_p^2} + \Delta\Sigma_{2h}, \quad (5)$$

where the first term is the one halo term taking into account the possibility that central galaxies may not be located at the centers of their host halos, the second term is the contribution from the stellar mass of the central galaxy, and the third term is the projected two-halo term. Since we only apply the method to central galaxies, cAGN and cAGN $_{\sigma_*}$ and their control galaxies, we do not include the satellite component.

Yang et al. (2006) provided the analytical formulae to calculate the ESD of the one-halo term from a NFW profile (Navarro et al. 1997) that is specified by two free parameters, the halo mass M_h and the concentration. We adopt their formula for the ESD with an additional parameter, R_{off} , that specifies the projected off-center distance. Following the model proposed by Johnston et al. (2007), we describe R_{off} by a two-dimensional Gaussian distribution with mean equal to zero and dispersion given by σ_{off} . To model the two-halo term, we first use CAMB² (Code for Anisotropies from Microwave Background) (Lewis & Challinor 2011) and the mcfits³ package (Li 2019) to obtain the matter correlation function, $\xi_{\text{mm}}(r)$. We then use the halo bias model of Tinker et al. (2010) to obtain the bias factor, $b_h(M_h)$, and to calculate the halo-matter cross-correlation function, $\xi_{\text{hm}}(r) = b_h \xi_{\text{mm}}(r)$. The projected two-halo term is obtained directly from ξ_{hm} (Cacciato et al. 2009). Finally, the stellar component is modelled as a point source and the stellar mass parameter is fixed as the mean value of M_* of the galaxy sample. We refer the reader to Luo et al. (2018) for a detailed description about the modelling of the three components.

Thus, model M1 consists of three free parameters, halo mass M_h , halo concentration and σ_{off} . We use emcee⁴ (Foreman-Mackey et al. 2013) to run a Monte Carlo Markov Chain (hereafter MCMC) to constrain these parameters, assuming the following likelihood function,

$$\ln(\mathcal{L}1) = -\frac{1}{2}(\Delta\Sigma_l - \Delta\Sigma_m)^T C_1^{-1}(\Delta\Sigma_l - \Delta\Sigma_m), \quad (6)$$

² <https://camb.info/>

³ <https://github.com/eelregit/mcfits/>

⁴ <https://emcee.readthedocs.io/en/stable/>

where $\Delta\Sigma_l$ and $\Delta\Sigma_m$ represent the true lensing signal and the model, respectively, and C_1^{-1} is the inverse of the covariance matrix. We only use the trace components of the covariance matrix to construct the likelihood function for the following two reasons. First, at scales smaller than our ESD measurements, shape noise dominates the error budget. Second, the covariance matrix is too noisy to be modeled reliably (Viola et al. 2015). The priors of the three parameters are set to be flat, with the halo mass in the range [11.0, 16.0] in logarithmic space, the concentration in the range [1.0, 16.0], and σ_{off} in the range of [0.001, 0.3] in units of the virial radius. In running the emcee, we use 300 walkers and run a chain of 5000 steps with 500 burn-in steps, starting from an initial setting of the three parameters, $\log(M_h/h^{-1}M_\odot) = 12.8$, concentration = 7.9, and $\sigma_{\text{off}} = 0.09$.

For the second model (hereafter M2), we combine the results from weak lensing and 2PCCF to constrain the halo mass. Different from M1, here we use the MCMC to fit the lensing results of cAGN, cSF^c and cQ^c simultaneously, and use the ratios of the 2PCCFs at large scales between the three samples as additional constraints. To this end, we use the halo mass estimated at each MCMC chain step to calculate the halo bias from the analytical formula given in Tinker et al. (2010). We then obtain the model bias ratios, cAGN/cSF^c and cAGN/cQ^c, and fit them to the corresponding ratios obtained from the observed 2PCCF. The likelihood function for the bias term is similar to Equation (6), except that the covariance matrix C_2 is built from bootstrap sampling,

$$\ln(\mathcal{R}) = -\frac{1}{2}(R_{w_p} - R_{\text{hb}})^T C_2^{-1}(R_{w_p} - R_{\text{hb}}), \quad (7)$$

where R_{hb} and R_{w_p} are the model bias ratio and the 2PCCF ratio between AGNs and the corresponding control sample, respectively. We only use the 2PCCF ratios on large-scales in the fitting: $r_p > 1 h^{-1}\text{Mpc}$ for cAGN/cSF^c and $r_p > 4 h^{-1}\text{Mpc}$ for cAGN/cQ^c. The reason for these choices and the robustness of the method are described in Section 4.2.

Model M2 is thus described by five likelihood terms in each MCMC step, three from the weak-lensing constraints and two from the 2PCCF ratios:

$$\begin{aligned} \ln(\mathcal{L}2) &= \ln(\mathcal{L}1)_{\text{cAGN}} + \ln(\mathcal{L}1)_{\text{cSF}^c} + \ln(\mathcal{L}1)_{\text{cQ}^c} \\ &+ \ln(\mathcal{R})_{\text{cAGN/cSF}^c} + \ln(\mathcal{R})_{\text{cAGN/cQ}^c}, \end{aligned} \quad (8)$$

The value of $\ln(\mathcal{L}2)$ at a given step is returned to the MCMC to decide the next chain step. The priors of M_h , concentration and σ_{off} and the initial settings of the MCMC for M2 are the same as for M1.

3. Properties of AGN host galaxies in comparison to normal star-forming and quiescent galaxies

Figure 1 shows the probability distribution functions (PDFs) of the specific star formation rate (sSFR), color (as indicated by $(g-r)^{0.1}$), D_n4000 and σ_* separately for AGN host galaxies, star-forming and quiescent galaxies, in four stellar mass bins. Here results are shown for cAGN (central AGNs) and the two control samples, cSF^c and cQ^c, as defined in Section 2.1. By definition, quiescent galaxies have

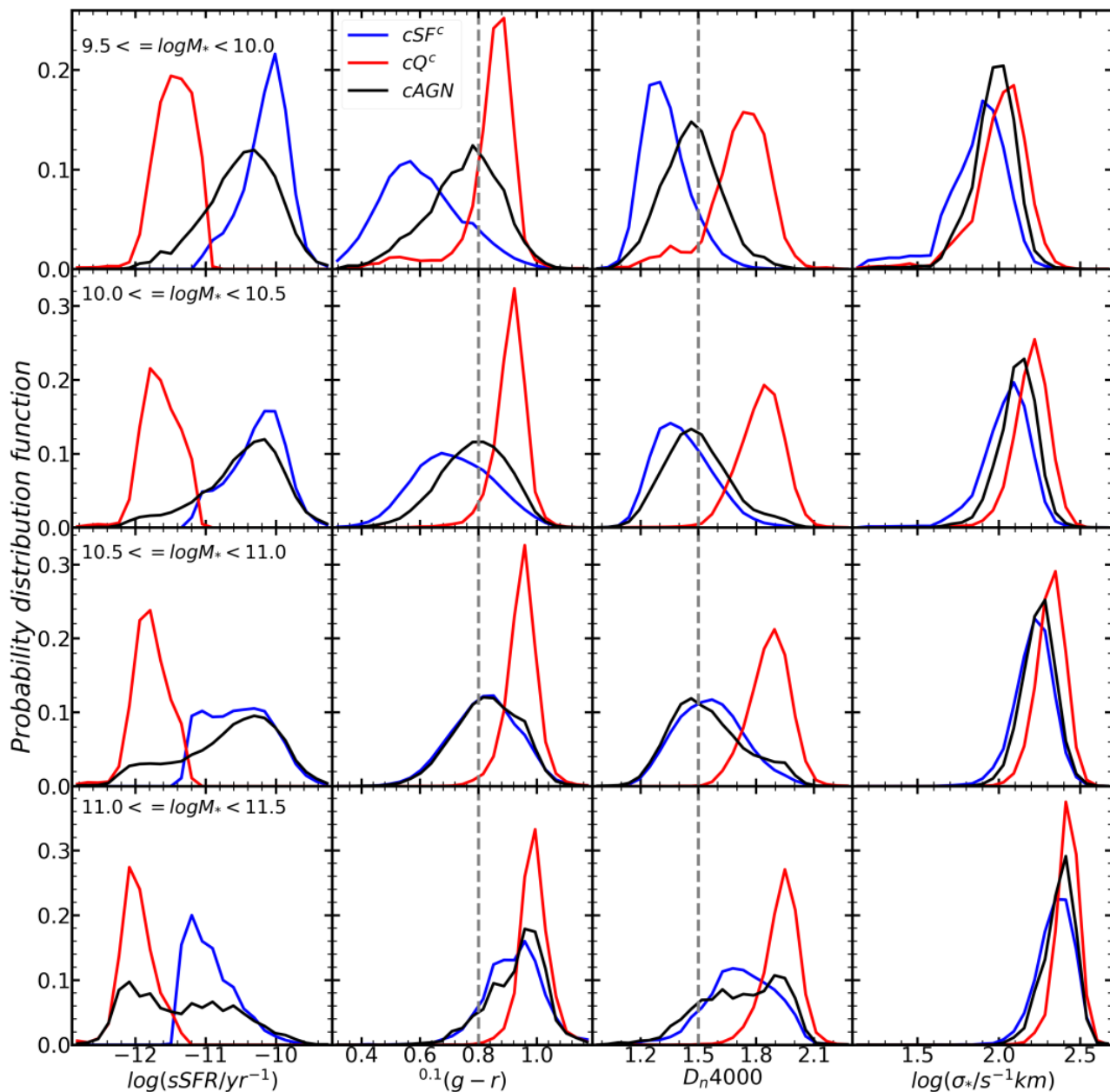


Fig. 1. The probability distribution functions in different stellar mass bins (as indicated in each row) of sSFR, color, D_n4000 and central velocity dispersion (each column) for cAGN (black), cSF^c (blue) and cQ^c (red). In the middle two columns, the vertical dashed lines (grey) show $^{0.1}(g-r)=0.8$ (second column) and $D_n4000=1.5$ (third column).

lower sSFR than star-forming galaxies, and the two populations have almost no overlap in their sSFR distributions within individual stellar mass bins. Because of the strong correlation of sSFR with color and D_n4000 , quiescent galaxies have higher $(g-r)^{0.1}$ and D_n4000 than star-forming galaxies. Quiescent galaxies also have larger σ_* than star-forming galaxies of the same stellar mass, consistent with the fact that the fraction of quiescent galaxies increases rapidly with σ_* (Bluck et al. 2016; Wang et al. 2018a). In addition, the color and D_n4000 for both populations increase gradually with stellar mass, because galaxies of lower masses in general are younger and metal poorer.

Compared to the control star-forming and quiescent galaxies, AGN host galaxies have a broad sSFR distribution that extends to both star-forming and quiescent regions.

However, the interpretation of this result is not straightforward, because the SFR estimates for AGNs may have larger uncertainties (see Brinchmann et al. 2004, for details.). The velocity dispersion distribution for AGNs is between the two control samples, suggesting that the supermassive black hole (SMBH) mass (M_{BH}) and the bulge mass of AGN hosts lie between the star-forming and quiescent populations. The difference between the AGN host galaxies and the star-forming galaxies becomes smaller as stellar mass increases. The color and D_n4000 distributions show similar trends, with the AGN host galaxies lying between the star-forming and quiescent populations. These results are in broad agreement with previous investigations (e.g. Man et al. 2019; Dodd et al. 2020), which found that AGN host galaxies tend to be in the green valley.

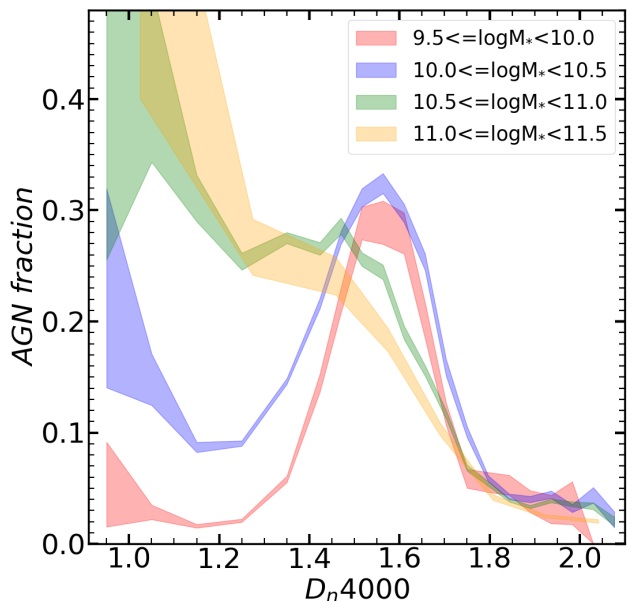


Fig. 2. AGN fraction in central galaxies as a function of D_n4000 in four stellar mass bins as indicated by different colors. The shaded regions represent the scatter of the fraction which is calculated by using 100 bootstrap samples. Note that V_{\max} correction is used in calculating the fraction. See text for details.

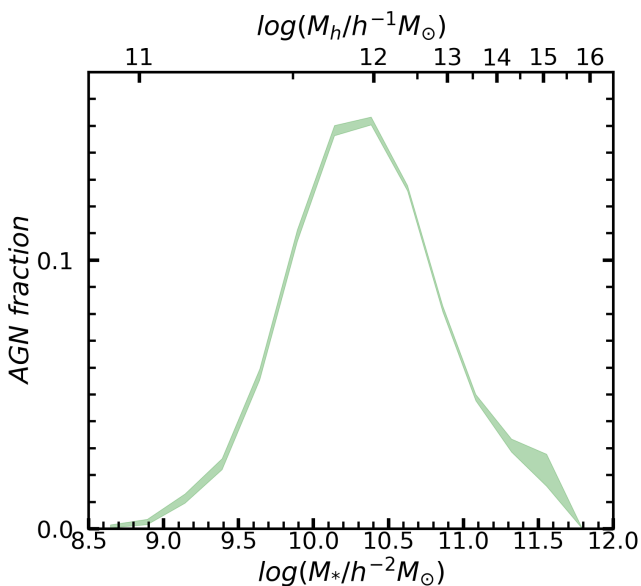


Fig. 3. V_{\max} corrected AGN fraction in central galaxies as a function of stellar mass. The top axis is the corresponding halo mass inferred by the stellar mass - halo mass relation in Yang et al. (2009). The shaded region represents the bootstrap error estimated by 100 samples.

Inspecting the PDFs in details, one can notice some interesting features. As a reference, the vertical dashed lines indicate $(g-r)^{0.1} = 0.8$ and $D_n4000 = 1.5$ in different panels of stellar mass bins. One can see that the peak positions of the $(g-r)^{0.1}$ and D_n4000 distributions for AGN host galaxies are almost independent of stellar mass over the range $9.5 < \log(M_*/M_\odot) < 11$. The only exception is

for the most massive galaxies, where AGN hosts on average are redder and have larger D_n4000 than their lower-mass counterparts. The difference is likely produced by the rise of a sub-population that has stellar populations similar to quiescent galaxies. This sub-population can also be seen in the other three mass bins, albeit less prominent. Thus, there seem to be two different AGN populations, at least for massive galaxies. One has color and D_n4000 similar to quiescent galaxies, and this population becomes important for AGNs hosted by massive galaxies. The other population, which is a dominant AGN population, has color and D_n4000 distributions that are independent of stellar mass. Note that for normal galaxies both the color and D_n4000 distributions shift to the redder and higher- D_n4000 sides with increasing stellar mass, and the trend is particularly strong for star-forming galaxies. The mass-independence of the color and D_n4000 distributions for the AGN population with $\log(M_*/M_\odot) < 11$ thus indicates that AGN host galaxies do not always lie in between star-forming and quiescent galaxies. It is likely that AGN hosts experienced a specific stage.

Figure 2 shows the AGN fraction as a function of D_n4000 in four stellar mass bins. Here, the AGN fraction is calculated by using the whole central galaxy sample (cG) with V_{\max} weighting (Blanton & Roweis 2007) and correction for redshift incompleteness (Blanton et al. 2005). The results clearly show two peaks, one at $D_n4000 \sim 1.0$ and the other at $D_n4000 \sim 1.5$. The peak height at $D_n4000 \sim 1$ depends strongly on stellar mass: for galaxies with $\log(M_*/h^{-2}M_\odot) > 10$, the AGN fraction is about 20% to 40%, and the fraction declines to 5% at the lowest stellar mass bin. In contrast, the second peak depends only weakly on stellar mass, with a value of about 30%. We show the AGN fraction as a function of stellar mass for central galaxies in Figure 3. AGN fraction is a strong function of stellar mass and peaks at stellar mass of about $10^{10.4} h^{-2}M_\odot$. The lower fraction at low (high) mass end reflects that these galaxies are dominated by star-forming and small D_n4000 (quiescent and high D_n4000) galaxies. The mean AGN fraction in the four stellar mass bins are about 8%, 15%, 11% and 5%, respectively. The fractions in the two D_n4000 peaks are much higher than the mean values, suggesting that AGNs tend to be hosted by galaxies in some specific evolution stages.

The low value, $D_n4000 \sim 1$, of the first peak signifies the existence of a very young stellar population in the central parts of the host galaxies.⁵ As shown in Kauffmann et al. (2003b) and Greene et al. (2020), the stellar age corresponding to $D_n4000 \sim 1$ is typically smaller than 10^8 years, indicating that the stars in the central parts of these galaxies formed through short bursts. Because of the short time scale, galaxies observed with such a young stellar population are rare, which may explain the absence of the peak in the PDFs shown in Figure 1. The peak at $D_n4000 = 1$, therefore, suggests that galaxies with strong current star formation have a strong tendency to be AGNs hosts. This is consistent with the result of Greene et al. (2020), who found that the fraction of AGN hosts among star-burst galaxies is high, and suggests that the process associated with a star burst may trigger AGN activities.

⁵ Note that SDSS fiber size limits the aperture over which the light from a galaxy is collected.

Table 1. Halo masses derived using lensing and clustering measurements for AGNs and their control samples.

Sample name	$\log M_*$	$\log M_h$ (M1)	$\log M_h$ (M2)
cAGN	All	$11.85^{+0.15}_{-0.19}$	$11.96^{+0.06}_{-0.07}$
cSF ^c		$11.85^{+0.07}_{-0.08}$	$11.81^{+0.06}_{-0.07}$
cQ ^c		$12.38^{+0.1}_{-0.06}$	$12.39^{+0.07}_{-0.05}$
cAGN	[9.5,10.0]	$11.68^{+0.42}_{-0.44}$	$11.63^{+0.23}_{-0.26}$
	[10.0,10.5]	$11.45^{+0.32}_{-0.3}$	$11.68^{+0.1}_{-0.11}$
	[10.5,11.0]	$12.08^{+0.2}_{-0.27}$	$12.1^{+0.08}_{-0.08}$
	[11.0,11.5]	$12.85^{+0.23}_{-0.3}$	$12.91^{+0.12}_{-0.12}$
cSF ^c	[9.5,10.0]	$11.85^{+0.22}_{-0.34}$	$11.39^{+0.3}_{-0.26}$
	[10.0,10.5]	$11.69^{+0.15}_{-0.2}$	$11.64^{+0.11}_{-0.13}$
	[10.5,11.0]	$11.9^{+0.13}_{-0.16}$	$11.88^{+0.1}_{-0.11}$
	[11.0,11.5]	$13.12^{+0.12}_{-0.14}$	$12.99^{+0.1}_{-0.11}$
cQ ^c	[9.5,10.0]	$11.83^{+0.33}_{-0.45}$	$12.17^{+0.16}_{-0.18}$
	[10.0,10.5]	$12.14^{+0.11}_{-0.1}$	$12.16^{+0.07}_{-0.07}$
	[10.5,11.0]	$12.43^{+0.07}_{-0.08}$	$12.44^{+0.06}_{-0.06}$
	[11.0,11.5]	$13.11^{+0.11}_{-0.1}$	$13.22^{+0.12}_{-0.09}$
cAGN _{σ_*}	All	$11.75^{+0.18}_{-0.23}$	$11.92^{+0.08}_{-0.08}$
cSF ^{c2} _{σ_*}		$11.73^{+0.09}_{-0.09}$	$11.76^{+0.08}_{-0.08}$
cQ ^{c2} _{σ_*}		$12.22^{+0.13}_{-0.08}$	$12.32^{+0.08}_{-0.07}$
cAGN _{σ_*}	[9.5,10.0]	$11.63^{+0.43}_{-0.41}$	$11.69^{+0.22}_{-0.25}$
	[10.0,10.5]	$11.44^{+0.31}_{-0.29}$	$11.73^{+0.11}_{-0.12}$
	[10.5,11.0]	$12.04^{+0.21}_{-0.31}$	$12.13^{+0.08}_{-0.08}$
	[11.0,11.5]	$12.77^{+0.26}_{-0.4}$	$13.12^{+0.11}_{-0.11}$
cSF ^{c2} _{σ_*}	[9.5,10.0]	$11.69^{+0.34}_{-0.41}$	$11.47^{+0.3}_{-0.29}$
	[10.0,10.5]	$11.72^{+0.13}_{-0.16}$	$11.72^{+0.11}_{-0.12}$
	[10.5,11.0]	$11.97^{+0.12}_{-0.14}$	$11.97^{+0.09}_{-0.1}$
	[11.0,11.5]	$13.23^{+0.08}_{-0.1}$	$13.4^{+0.09}_{-0.1}$
cQ ^{c2} _{σ_*}	[9.5,10.0]	$11.97^{+0.28}_{-0.44}$	$12.21^{+0.15}_{-0.18}$
	[10.0,10.5]	$12.11^{+0.14}_{-0.12}$	$12.16^{+0.09}_{-0.09}$
	[10.5,11.0]	$12.27^{+0.09}_{-0.1}$	$12.32^{+0.07}_{-0.07}$
	[11.0,11.5]	$13.07^{+0.12}_{-0.14}$	$13.15^{+0.09}_{-0.1}$

The second peak at $D_n4000 \sim 1.5$ corresponds to the dominant AGN population shown in Figure 1. This peak was not found in Greene et al. (2020), because they only focused on star burst galaxies and their sample contained only few galaxies with $D_n4000 \geq 1.5$. Kauffmann et al. (2003a) studied the H δ absorption lines of AGN host galaxies and found that a significant fraction of them have experienced a star burst phase within the past 1-2 Gyrs. Thus, the host galaxies of AGNs in this peak may have also been triggered by a processes associated with a star burst. However, since the life time for AGN activities is believed to be less than 10^8 years (e.g. Marconi et al. 2004; Schawinski et al. 2015; Yuan et al. 2018), the observed AGNs in this peak cannot be directly related to the star bursts that happened 1 to 2 Gyrs ago. We will come back to the implications of this results later.

4. Masses of AGN Host Halos

In Section 2, we described how one can estimate the host halo mass of central galaxies using gravitational lensing signals and the 2PCCF. Here we apply the methods to AGNs and the corresponding control samples of normal galaxies

to investigate the masses of AGN host halos in comparison to those of normal galaxies.

4.1. Results from galaxy-galaxy lensing

In Figure 4, we show the excess surface density profiles derived from the g-g lensing signal for sample cAGN and corresponding control samples cSF^c and cQ^c. As one can see, the ESD profiles obtained from cAGN and cSF^c are quite similar, while that for cQ^c is higher. To quantify the results, We use model M1 (see Section 2.3 and also Luo et al. (2018)) to fit the observed ESD profiles and to derive an average halo mass for each of the three samples. The results of the halo mass are listed in Table 1. The halo mass for central AGNs is about $10^{11.85} h^{-1} M_\odot$, in agreement with the g-g lensing results for AGNs selected from the SDSS DR4 (e.g. Mandelbaum et al. 2009). The halo mass for the control sample of star-forming galaxies, cSF^c, is very similar to that of AGNs, while the mean halo mass for the quiescent galaxies, about $10^{12.38} h^{-1} M_\odot$, is about three times as high as those for AGNs and star-forming galaxies of the same stellar mass. We have also carried out the same analysis for AGN hosts and normal galaxies in four stellar mass bins, and corresponding results are listed in Table 1 and plotted in Figure 5. As expected, for each population, the average halo mass is larger for galaxies with larger stellar masses. For a given stellar mass, the average halo masses for AGN hosts and star-forming galaxies are similar but lower than that of quiescent galaxies.

Because of the limit by the sample size, the halo masses obtained from the g-g lensing measurements are quite uncertain, particularly when galaxies are divided into sub-samples of stellar mass. However, additional constraints on halo mass can also be obtained through halo bias estimated from the clustering strength on large scales. In what follows, we present results based on the clustering measurements.

4.2. Constraints from 2PCCF

Figure 6 shows the projected 2PCCFs, $w_p(r_p)$, for central AGNs (cAGN) in comparison to the corresponding control galaxies. The 2PCCFs of the three samples exhibit some interesting features on both small and large scales. We will talk about the small-scale in the next section; here we focus on the properties on large scales in connection their implications for halo masses. As one can see, AGNs have almost the same clustering amplitude as the control star-forming galaxies at scales larger than about $0.4 h^{-1} \text{Mpc}$, suggesting that the host halos for the two populations have very similar large-scale bias and halo mass. At scales larger than $\sim 4 h^{-1} \text{Mpc}$, the cAGN/cQ^c ratio is almost a constant and is less than one, indicating that quiescent galaxies reside in more massive halos than both AGNs and star-forming galaxies. We have also estimated the 2PCCF results for galaxies in the same four stellar mass bins as used in the g-g lensing analysis, and the results are shown in Figure 7. The results are consistent with those shown in Figure 6. At large scales, cQ^c are more strongly clustered than both cAGN and cSF^c, and cAGN has the same clustering strength as cSF^c.

The results obtained from the 2PCCFs on large scales are thus consistent with the interpretation of the g-g lensing results in terms of halo mass. Using the halo masses derived

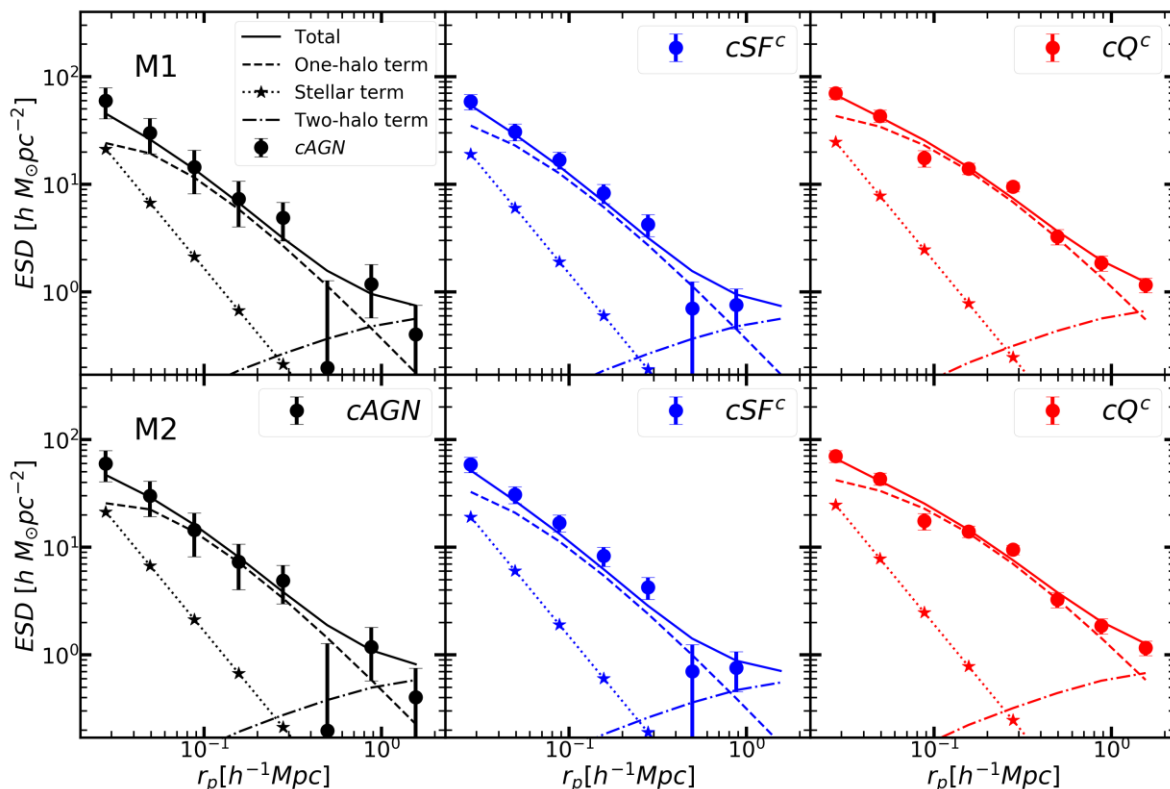


Fig. 4. The lensing signal and the best fitting results for cAGN (black, left column), cSF^c (blue, middle column) and cQ^c (red, right column) with different methods (the upper row is for M1, the lower row for M2). In each panel, the dots with error bars are the lensing signal, while the dashed line, dotted line with stars and point line represent contribution from one-halo term, stellar mass term and two-halo term, respectively. The total fitting result is indicated by the solid line.

from the lensing (M1 method) and the theoretical model for halo bias described in Tinker et al. (2010), we can predict the ratio of the 2PCCF on large scales between cAGN and cQ^c. The ratios for different cases are shown as the horizontal dashed lines in Figure 6 and the corresponding panels of Figure 7. We see that the lensing and clustering results are in good agreement for the three high mass bins. The discrepancy for the lowest mass bin is difficult to judge, as the uncertainties for both measurements are large.

The good agreement between the lensing and clustering results suggests that we can combine the results to obtain tighter constraints on halo masses using model M2 described in Section 2.3. Since cAGN and cSF^c have a similar cross correlation amplitude on scales larger than $\sim 1 h^{-1} \text{Mpc}$, and the ratio of the 2PCCF between cAGN and cQ^c is roughly a constant at scales larger than $\sim 4 h^{-1} \text{Mpc}$, the likelihood terms for the 2PCCF (Equation 7) are calculated using the ratios at $r_p > 1 h^{-1} \text{Mpc}$ for cAGN/cSF^c and at $r_p > 4 h^{-1} \text{Mpc}$ for cAGN/cQ^c. For comparison, the best-fitting models to the ESD profiles are shown in the lower panels of Figure 4, and the derived halo masses are given in Table 1. As one can see, the halo masses derived from model M2 agree very well with those from M1, indicating again that the lensing and clustering results are consistent with each other. The combined constraints also lead to smaller uncertainties, as expected.

The stellar mass - halo mass relation (SHMR) obtained from model M2 is shown in Figure 5. For comparison, the result for the total central sample, cG, obtained using model M1 is shown as green points. As references, the SHMR de-

rived by various methods in the literature, including galaxy group catalog (Yang et al. 2009), abundance matching (see e.g. Moster et al. 2010; Behroozi et al. 2019), conditional luminosity function (Kravtsov et al. 2018) and weak lensing (Leauthaud et al. 2012) are presented. Our result for the total sample is in good agreement with previous results, indicating that our method is reliable. In general, the halo mass increases with stellar mass. And there is a pivot halo mass around $10^{12} h^{-1} M_{\odot}$, above and below which the SHMR have different slopes.

Our analysis, combining weak lensing and clustering measurement, clearly show that, at given M_* , the host halos of quiescent galaxies are more massive than those of star-forming galaxies and AGN host galaxies. The difference is particularly significant in the two middle M_* bins, which include most (about 88%) of the AGNs. It is in agreement with previous studies that found quiescent galaxies reside in more massive halos than star-forming galaxies of the same M_* (e.g. Mandelbaum et al. 2006; Behroozi et al. 2019). It is broadly consistent with the passive quenching model (Wechsler & Tinker 2018), in which star-forming galaxies grow faster than quiescent galaxies, while their host halos grow in a statistically similar manner. The host halo masses of AGN host are in good agreement with those for star-forming galaxies, indicating that the two populations of galaxies may be connected, as we will discuss in Section 6.

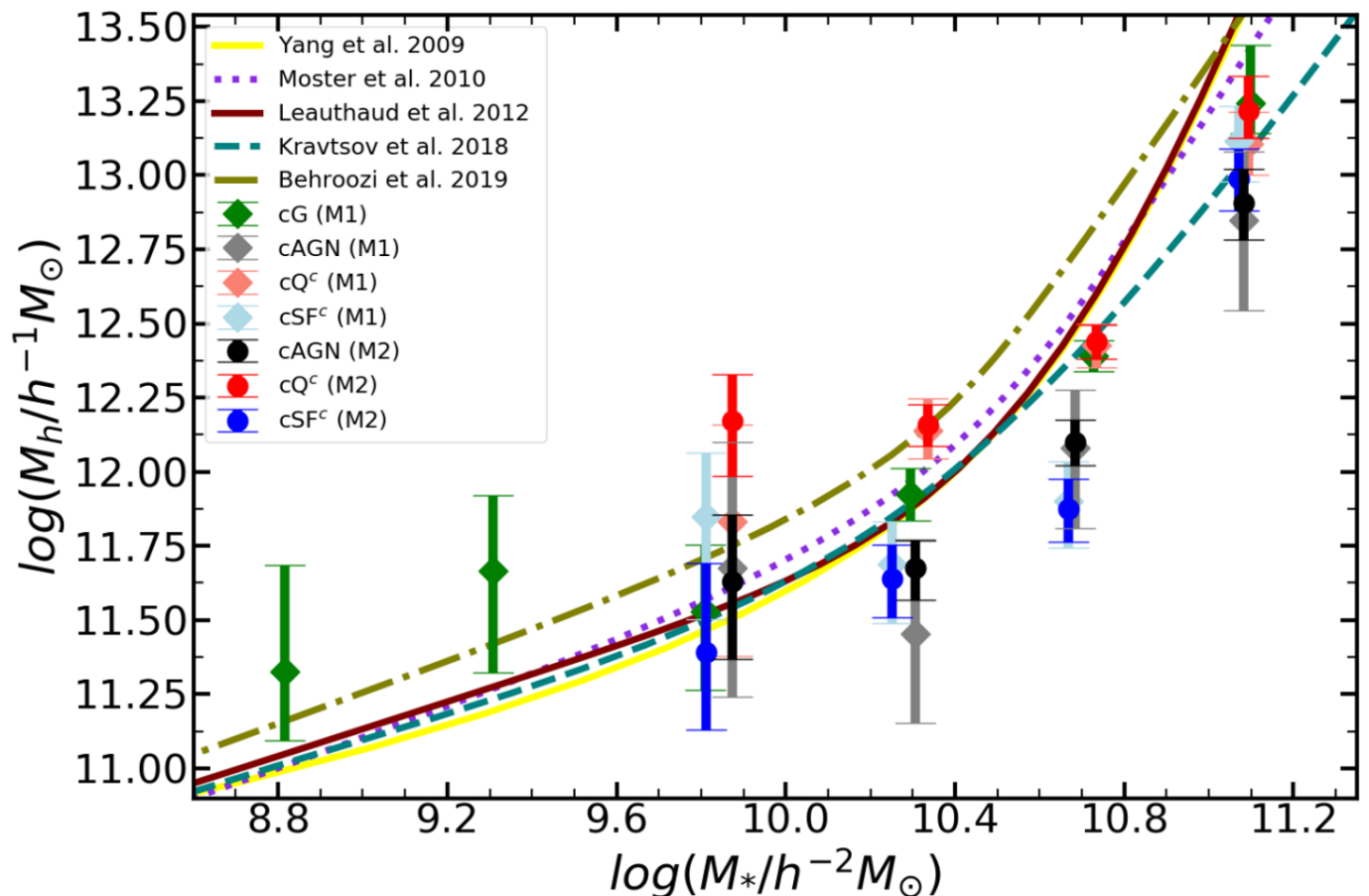


Fig. 5. Stellar mass-halo mass relation for central AGNs and their control galaxies. For our results, those halo masses derived by M1 are given by diamonds with error bars, while those derived by M2 are given by dots with error bars. For comparison, we also show the SHMR in the literature, obtained by using various methods, including galaxy group catalog (Yang et al. 2009), abundance matching (see e.g. Moster et al. 2010; Behroozi et al. 2019), conditional luminosity function (Kravtsov et al. 2018), and weak lensing (Leauthaud et al. 2012).

5. Satellite Galaxies around AGNs

In the last section, we have shown that the masses of AGN halos are similar to those of star-forming galaxies of the same stellar mass. In this section, we examine further whether or not the host halos of AGNs and star-forming galaxies may be different in the number of satellite galaxies they contain. The answer to this question may shed light on the roles of galaxy-galaxy interaction in triggering AGN activities. In the literature, there are suggestions that the AGN activities may depend on the central velocity dispersion of galaxies. We therefore also check whether or not the satellite abundance depends on the central velocity dispersion of the central galaxies.

5.1. Excess of satellites around AGNs

As shown in the left panels of Figure 6, AGNs are more strongly clustered than star-forming galaxies at small scales, although both populations have similar 2PCCF on large scales. At $r_p < 300 h^{-1} \text{kpc}$, the ratio in 2PCCF between cAGN and cSF^c increases and reaches about 1.5. The mean halo mass for the two samples, which is about $10^{11.96} h^{-1} M_\odot$, corresponds to a mean halo virial radius, $r_{\text{vir}} \approx 0.26 h^{-1} \text{Mpc}$, and is indicated by the vertical dotted line. As one can see, the virial radius separates the 2PCCF

into two distinct parts. The slope of $w_p(r_p)$ becomes much steeper at scales smaller than the virial radius, and this is true for both the AGN and star-forming samples. This reflects the transition of the correlation function from one-halo to two-halo terms, providing an additional support to the reliability of our halo mass estimate. Within the virial radius, the cross correlation strength for AGNs is enhanced relative to that for star-forming galaxies, indicating that the average number of satellites around AGNs is higher than that around central star-forming galaxies. + The results shown in Figure 7 for galaxies in four different stellar mass bins indicate that the enhancement of the correlation strength within the virial radius for AGNs is present in the two intermediate mass bins. In the lowest mass bin, there are only 3,604 cAGNs, making the error bars quite large. In the most massive bin, the enhancement seems to be insignificant. This might owe to the fact that a large fraction of the AGN host galaxies in this mass bin are quiescent galaxies, different from the main AGN population (see Section 3). However, because of the limited sample size (the number of cAGNs in the most massive bin is 1,634), we are not able to obtain a definite answer to this question. Based on the halo mass estimated for individual subsamples, we derive the corresponding virial radii and show them as the vertical dotted lines. Similar to Figure 6, the change of the slope of the 2PCCFs occurs around the virial radii and the

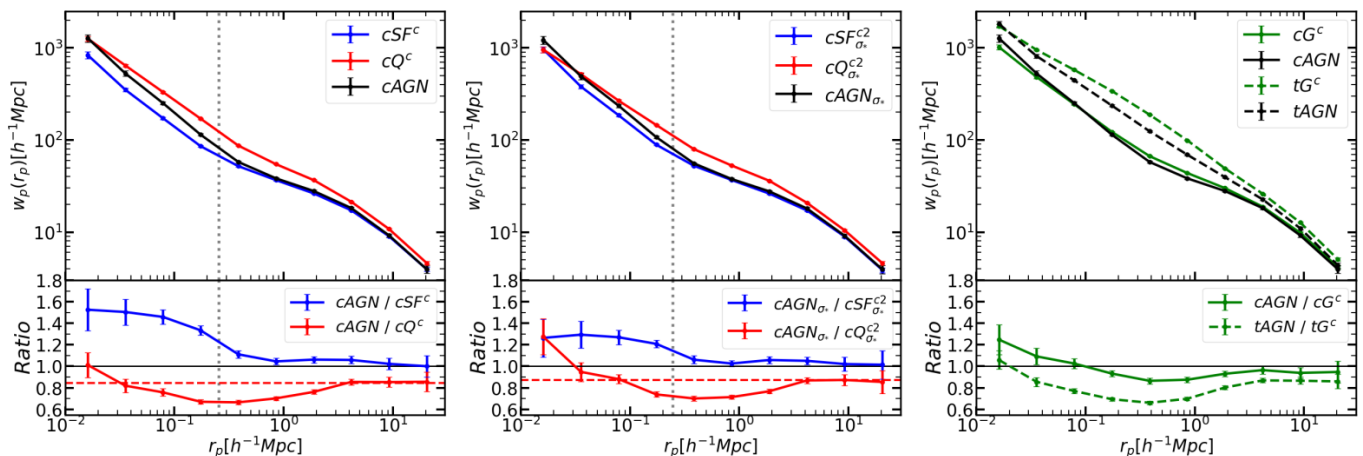


Fig. 6. Left panels: the upper panel shows the 2PCCF of cAGN (black) and its control star-forming (cSF^c) and quiescent galaxies (cQ^c). The lower panel shows the 2PCCF ratio of cAGN to cSF^c (blue) and cAGN to cQ^c (red). The horizontal dashed line (red) indicates the theoretical halo bias (Tinker et al. 2010) ratios between cAGN and cQ^c with halo mass derived by M1. The vertical dotted line (grey) indicates the virial radius of the host halo of cAGN derived by M2. Middle panels: Similar to the left panels, but for cAGN_{σ*} and their control galaxies, cSF_{σ*}^{c2} and cQ_{σ*}^{c2}. Right panels: upper panel shows the 2PCCF for cAGN and its control galaxies (cG^c), tAGN and its control galaxies (tG^c). The lower panel shows the 2PCCF ratio of cAGN to cG^c and tAGN to tG^c. Please see Section 2.1 for the sample construction.

enhancement of the 2PCCF for AGNs is found only within the virial radii.

To examine which kind of satellites contribute to the difference between AGNs and star-forming galaxies, we identify satellites around galaxies in cAGN and cSF^c as follows. For a given central AGN in cAGN or a star-forming galaxy in cSF^c, we select satellites from the reference galaxy sample according to the following criteria, $|\delta z| \leq 3v_{\text{vir}}/c$, $r_p \leq r_{\text{vir}}$ and $M_s < M_c$. Here r_{vir} and v_{vir} are, respectively, the virial radius and virial velocity calculated assuming a halo mass of $10^{11.96} h^{-1} M_\odot$, δz is the redshift difference between a central and a satellite, and M_c and M_s are the stellar masses of the central and satellite, respectively. We then compute the mean numbers of satellites around the central AGNs and star-forming galaxies, denoted by $N_{s,A}$ and $N_{s,S}$, respectively. The errors are calculated by using 100 bootstrap samples. Due to Malmquist bias, $N_{s,A}$ or $N_{s,S}$ does not represent the true number of satellites around the centrals. However, since cAGN and cSF are matched in redshift, the Malmquist bias is expected to have a similar effect on both so that the number ratio, $N_{s,A}/N_{s,S}$, should not be affected significantly. Figure 8 shows $N_{s,A}/N_{s,S}$ as a function of M_s (left panel) and M_s/M_c (right panel). The ratio, $N_{s,A}/N_{s,S}$, changes little with the satellite mass, except the small peak around $\log(M_s/h^{-2}M_\odot) = 9.7$. In contrast, the ratio changes strongly with M_s/M_c . The mean number of satellites around AGNs is similar to that around star-forming galaxies for satellites with stellar masses comparable to the centrals ($M_s/M_c \sim 1$). As M_s/M_c decreases, the number ratio increases rapidly to ~ 1.8 at $M_s/M_c = 0.1$ and remains almost constant down to $M_s/M_c = 0.001$. Thus, the difference in satellite abundance between central AGNs and star-forming galaxies is larger for satellites of lower masses relative to their centrals.

To summarize, our results clearly show that central AGNs are surrounded by more satellites, especially small satellites with masses less than about one-tenth of the central mass, than star-forming galaxies in the control sample. This suggests that local environments, as represented by

the abundance of satellites, play an important role in triggering AGN activity, as we will discuss later.

5.2. The effects of galaxy central velocity dispersion

In above sections, control samples are matched with AGN samples only in stellar mass and redshift. Since central velocity dispersion of galaxies, which is related to the mass of the central bulge, has been suggested as an important parameter related to galaxy quenching, it is interesting to investigate its impacts on our results. To this end, we examine cAGN_{σ*} in comparison with the corresponding control samples, cSF_{σ*}^{c2} and cQ_{σ*}^{c2}. As detailed in Section 2.1, these samples are constructed by matching them not only in stellar mass and redshift, but also in central velocity dispersion, σ_* . The analyses for these samples are the same as those described above. The average halo masses estimated from g-g lensing measurements using Models M1 and M2 are listed in Table 1, and the results about the projected 2PCCFs are shown in the middle panel of Figure 6.

As one can see, AGNs and control star-forming galaxies still have similar mean halo mass and clustering amplitude at large scales, even after σ_* is constrained. Here again, quiescent galaxies tend to reside in more massive halos and are more strongly clustered. The halo mass obtained from lensing measurements is consistent with that based on the clustering results, as shown by the horizontal dashed line, which indicates the prediction of the halo bias model using the lensing mass. In fact, controlling σ_* does not change the results on halo mass significantly (Table 1).

On small scales, $r_p < r_{\text{vir}}$, we can see a clear change in the slope of $w_p(r_p)$ at $r_p \sim r_{\text{vir}}$, and a significant excess in clustering strength for AGNs relative to the control star-forming galaxies. Thus, consistent with the results presented earlier, AGNs are surrounded by more satellites than are star-forming galaxies. However, the excess becomes smaller, with the ratio reduced to about 1.3, after σ_* is controlled. Figure 8 shows $N_{s,A}/N_{s,S}$ as a function of M_s and M_s/M_c for the new samples. Although the overall trend

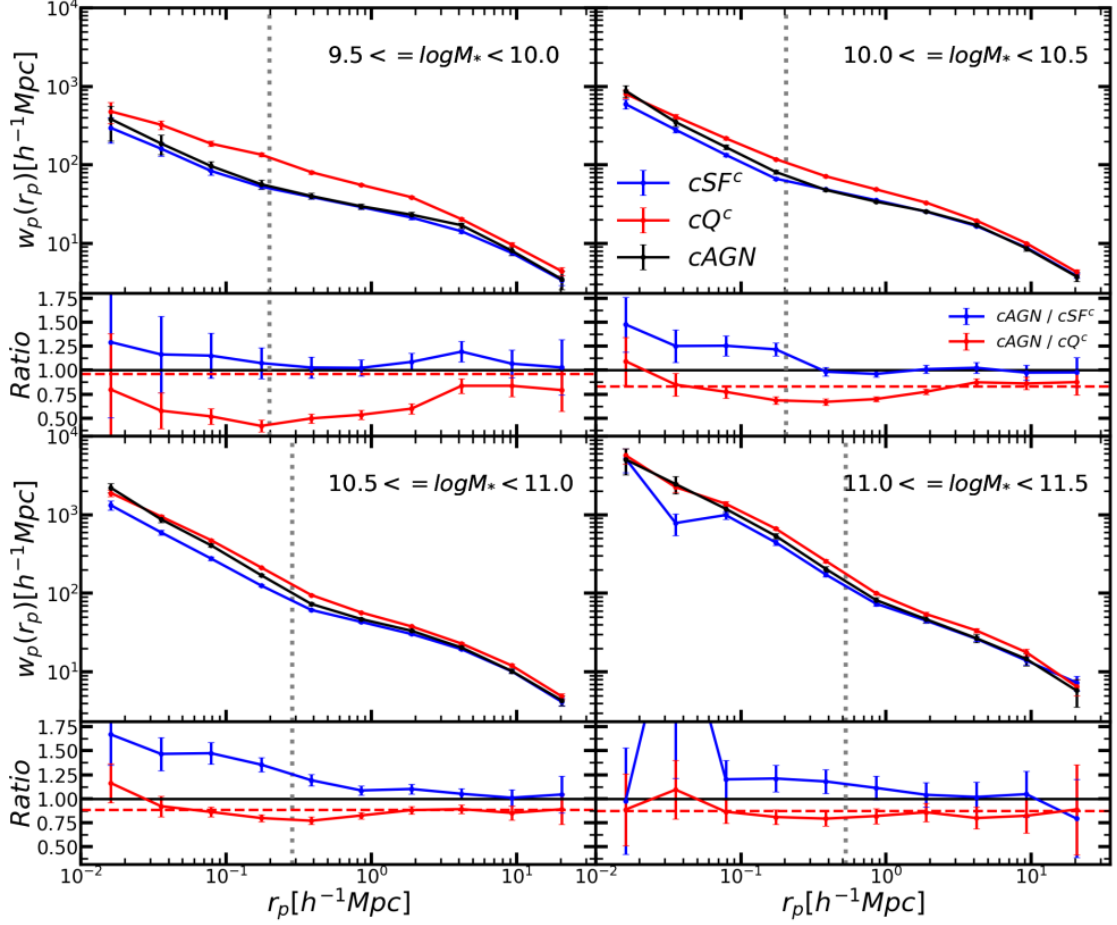


Fig. 7. Similar to the left panels in Figure 6, but $cAGN$, cQ^c and cSF^c are split into four stellar mass bins as indicated in each panel.

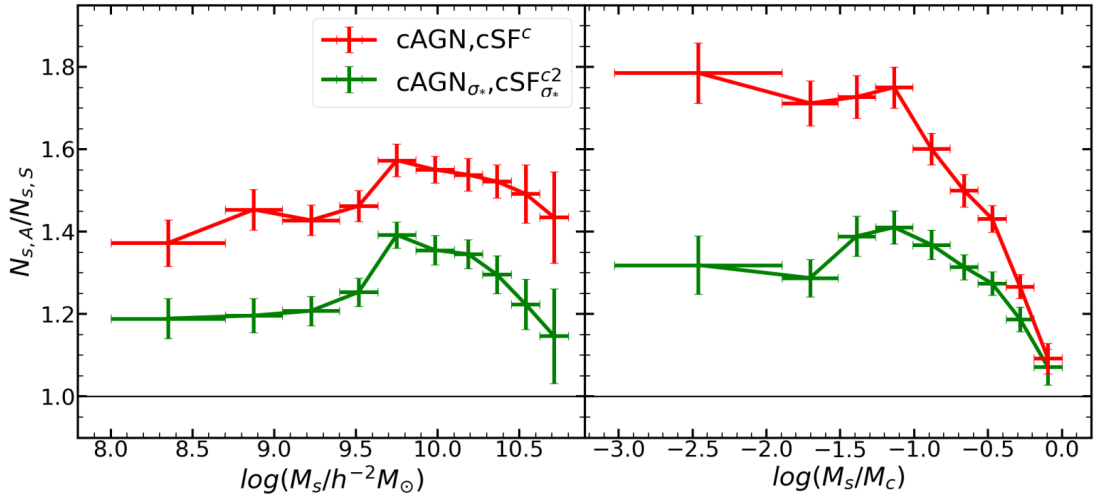


Fig. 8. The left panel shows the ratio of the mean satellite number around two $cAGN$ samples ($cAGN$ and $cAGN_{\sigma_*}$) over the mean satellite number around two corresponding control star-forming samples (cSF^c and $cSF_{\sigma_*}^{c2}$) as function of satellite stellar mass, respectively. The right panel is similar to the left, but the ratio is as function of satellite stellar mass (M_s) over central stellar mass (M_c).

is similar to that shown above, the ratio is smaller. For example, at $\log M_s/M_c = -1.0$, the mean number of satellites around AGNs is about 1.4 times that around star-forming galaxies.

To understand the new results, it is interesting to check whether or not galaxy clustering depends on σ_* for fixed stellar mass. As shown in Section 2.1, there is a small difference between $cAGN_{\sigma_*}$ and $cAGN$ samples. To have a fair comparison, we construct two additional control samples,

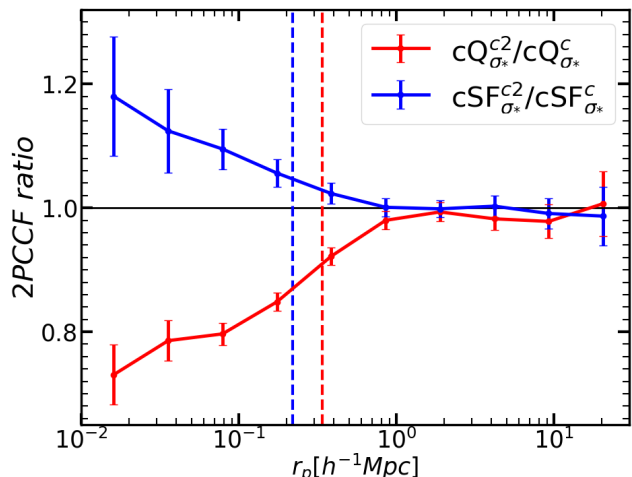


Fig. 9. The 2PCCF ratio of $cQ_{\sigma_*}^{c2}/cQ_{\sigma_*}^c$ (red) and $cSF_{\sigma_*}^{c2}/cSF_{\sigma_*}^c$ (blue). The red and blue vertical dashed line represent the virial radius of host halos for $cQ_{\sigma_*}^{c2}$ and $cSF_{\sigma_*}^{c2}$ derived by M2, respectively. See Section 5.2 for the details of the construction of the control samples.

$cSF_{\sigma_*}^c$ and $cQ_{\sigma_*}^c$, for $cAGN_{\sigma_*}$, by only matching M_* and z . Figure 9 shows the 2PCCF ratios between the control samples with and without controlling σ_* , respectively. For star-forming and quiescent galaxies, controlling σ_* does not change the clustering at the scales larger than the virial radius, consistent with our halo mass measurement. At scales less than the virial radius (indicated by the vertical dashed lines), however, $cQ_{\sigma_*}^c$ more strongly clustered than $cQ_{\sigma_*}^{c2}$, while $cSF_{\sigma_*}^c$ is less strongly correlated than $cSF_{\sigma_*}^{c2}$. Since on average the AGN sample has smaller σ_* than the quiescent sample, but larger σ_* than the star-forming one, as shown in Figure 1, these two results indicate that, at given stellar mass, galaxies with higher σ_* are surrounded by more satellites. This suggests that the present of satellite galaxies may play a role in the buildup of bulges. It suggests that the bulge formation and AGN activities may be caused by the same mechanism. We will come back to this issue in Section 6.4.

6. Discussions and Implications

6.1. Impact of the AGN sample selection

AGNs used in our analysis are identified from the SDSS galaxy main sample based on narrow emission lines. AGNs with weak or insignificant narrow lines, which may be produced by low black-hole activities, are not included. Moreover, the majority of the AGNs used here are type II AGNs, in which broad lines and continuum are expected to be blocked by dusty structures. Thus, type I AGNs that show broad lines are not included in our analysis. Furthermore, we consider only central AGNs. So selected, our AGN sample is a biased sample of the total AGN population. Detailed analyses are required to examine the potential impact of these selections; here we present some discussion about the issue.

According to the standard unified model (Antonucci 1993), the difference between type Is and IIs are attributed solely to orientation effects. In this case, ignoring type Is

should not significantly change our results. However, there is growing evidence against the unified model. For example, Jiang et al. (2016) and Powell et al. (2018) found that type Is have the same clustering as type IIs at large scales, but have significantly weaker clustering at small scales, indicating that they reside in halos of similar mass but with different satellite abundances. Thus, if type I AGNs were included in the analysis, the difference in small-scale clustering between AGNs and star-forming galaxies presented above would be reduced.

The typical [OIII] luminosity of our type II AGN sample is less than $10^{41} \text{ erg s}^{-1}$, at which the type I fraction is less than 20% (Simpson 2005; Khim & Yi 2017). This means that Type Is can only be a small part of the whole AGN sample, and that the impact of excluding type Is may not be large. However the selection effects for the two types are usually different, and different methods for constructing control samples are adopted in earlier studies. These make it difficult to estimate the impact of including Type Is. Moreover, the difference between the two types of AGNs indicates that they may be triggered by different processes (e.g. Jiang et al. 2016). Including type Is may, therefore, mix various effects, making it more difficult to understand the underlying processes. Given all of these, we believe that it is better to investigate the two populations separately.

We do not consider satellite AGNs, because satellites complicate the interpretations of the results. To demonstrate this, we show in the right panels of Figure 6 the 2PCCFs of the total AGN sample (tAGN), in comparison to the corresponding control galaxy sample, tG^c . As one can see, the correlation for tAGNs is weaker than that of the control sample on both small and large scales. At scales of hundreds of $h^{-1} \text{ kpc}$, there is a dip in the ratio between tAGN and tG^c (see e.g. Li et al. 2006b). Comparing to the results for centrals (green lines), we can see that including satellites enhances the difference between AGNs and normal galaxies on both small and large scales. One possible explanation is that the AGN fraction is lower among satellites than among centrals (e.g. Li et al. 2006b; Wang & Li 2019). Clearly, more effects have to be taken into account in order to explain results obtained from a mixture of centrals and satellites.

6.2. The importance of using well-defined control samples

Two galaxy properties are commonly adopted in the construction of control samples, one is galaxy stellar mass and the other is redshift. For investigations using flux-limited samples to measure the 2PCCF, as is carried out here, it is essential to match samples to be compared in redshift. Since the galaxy population covers a large range of stellar mass, and since many other properties are related to galaxy mass, controlling galaxy mass is necessary if one wants to separate effects caused by other properties from those caused by the mass. Other galaxy properties, such as color, D_n4000 and σ_* , are sometimes also used to control AGN and normal galaxy samples, to find differences that are not caused by these properties. However, inappropriate control samples can reduce the effects one is looking for. For example, if galaxy interaction can significantly affect the bulges, as indicated by the results in Section 5.2, controlling σ_* may lead to an underestimate of the role of the interaction. Similarly, if AGNs can strongly affect star formation in their hosts, comparing AGNs with normal galaxies that have sim-

ilar color and D_n4000 to AGN host galaxies might lead to biased results.

As shown in Section 6.4, our results suggest that the processes linked to AGNs may change the properties of their host galaxies. If we want to investigate whether or not galaxy environment has played an important role in these processes, galaxies in the control sample should be statistically similar to the progenitors of the AGN hosts (i.e. the host galaxies before the onset of the AGN) rather than the host galaxies on the AGN duty cycle. This suggests that we should select, as our comparison sample, normal galaxies that have the same properties as the AGN host galaxies before the onset of AGN. This is not straightforward to do but our results provide some hints. Since AGN hosts and star-forming galaxies share the same SHMR, controlling stellar mass is equivalent to controlling halo mass. Since the average formation history of central galaxies is determined by the host halo mass, star-forming galaxies controlled in stellar mass thus provide a comparison sample that we need to investigate whether or not the host galaxies of AGNs are special in their environment and evolutionary stages relative to the average population of galaxies. According to N -body simulations, halos of $10^{12} h^{-1} M_\odot$ at $z = 0$ assembled half of their mass at $z \sim 1$ (Wang et al. 2011a), and so the growth timescale for a $10^{12} h^{-1} M_\odot$ halo is typically about 7 Gyrs. This time scale is much longer than the time scale for the evolution between star-forming galaxies and AGNs, which is about 1-2 Gyrs according to the values of D_n4000 of AGN hosts and star-forming galaxies. This indicates that controlling halo mass also provides a stable reference to investigate evolution in star formation and AGN activities.

Since quiescent galaxies reside in more massive halos than AGN hosts of the same stellar mass, it is not appropriate to use them to form a comparison sample to investigate the host galaxies of AGNs in their environment and evolutionary stages relative to the average population. Note that only a small fraction, about 3 ~ 5 percents of galaxies with large D_n4000 , at which quenched galaxies dominate, have strong AGN activities (Figure 2). Assuming that quiescent galaxies are quenched long time ago, Man et al. (2019) also suggested the exclusion of quiescent galaxies in comparing AGNs with normal galaxies. Our results provide further justifications for such an approach.

Finally, we note that our control samples contain AGNs. In order to check whether the AGN contamination in the control samples can cause bias in our results, we repeat all of the analyses shown above by using control samples that exclude AGNs. Our tests show that the results change very little. This is expected, because only a small fraction of galaxies, between 5% and 15% (see Section 3), are identified as AGNs. For simplicity, we do not show them here.

6.3. Triggering AGN with minor interactions

Comparing with star-forming galaxies, we find that local environment plays a dramatic role in triggering AGN activity. In particular, we find that small satellites dominate the environmental difference between AGNs and star-forming galaxies. This suggests that minor interactions may be responsible for driving gas to flow into the galaxy center and trigger AGN activity. This does not mean that massive satellites can not trigger AGN activity, but that they are not dominating because they are rarer.

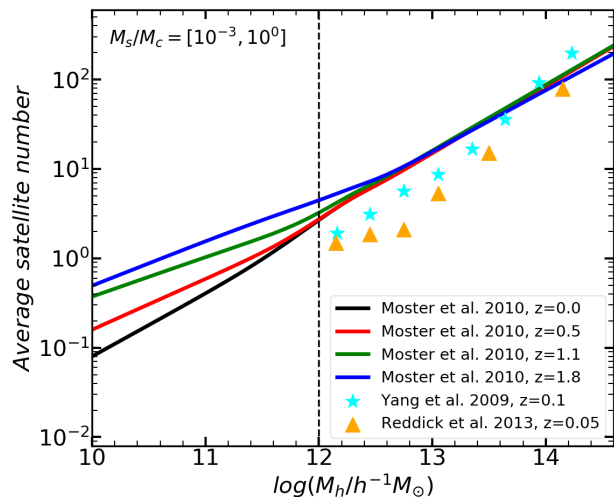


Fig. 10. The average number of satellite galaxies, with M_s in range of $[10^{-3}, 1]$ of M_c , as function of halo mass. Here, M_s and M_c are the masses of satellites and centrals. Four lines denote the results at four redshifts derived from the conditional stellar mass function (CSMF) shown in Moster et al. (2010). The triangles and stars represent the results derived from the CSMFs of Reddick et al. (2013) and Yang et al. (2009), respectively.

The probability for a central galaxy to interact with its satellites depends on the number of satellites within its host halo. Based on the conditional stellar mass function (CSMF) for satellites derived using group catalogs and the abundance matching methods (Yang et al. 2009; Moster et al. 2010; Reddick et al. 2013), we estimate the number of satellites with stellar masses, M_s , in the range of $[10^{-3}, 1] \times M_c$, where M_c is the stellar mass of the central galaxy, and show the results in Figure 10. The mean number of satellites per halo at $\log M_h/h^{-1} M_\odot = 12$ is of the order of unity at $z \sim 0$, and the variance among different methods is not too large. This means that central galaxies in these halos have a high probability, close to unity, to interact with their satellites with mass above $M_c/1000$ within an time scale, t_{it} . Since interaction requires that centrals and satellites are close enough, t_{it} is expected to be comparable to the merger timescale of galaxies. As shown in Jiang et al. (2008), merger time scale ranges from 1 Gyr to about 10 Gyrs, with a typical value of 3 Gyrs.

The number of satellites increases with halo mass. Thus, interaction is expected to be even more frequent for halos of mass larger than $10^{12} h^{-1} M_\odot$. However, in these halos, most of the central galaxies are quiescent galaxies, containing little cold gas, so such interactions may not produce AGNs. This, together with the fact the abundance of halos decreases with halo mass, implies that only a small fraction of optical AGNs reside in massive halos. For halos with $M_h \ll 10^{12} h^{-1} M_\odot$, the mean number of satellites is much smaller than unity, so that the interaction probability is also small. This suggests that the AGN fraction among low-mass galaxies should also be lower, even though they have plenty of cold gas and strong star formation. Figure 3 shows the AGN fraction as a function of halo mass, which is converted from AGN fraction as a function of stellar mass based on the SHMR in Yang et al. (2009). We can see that AGN fraction reaches maximum around $10^{12} h^{-1} M_\odot$ and

becomes much lower at the low and high halo mass end, consistent with our analysis. Note that the satellite number and t_{it} may vary significantly among individual halos of a given M_{h} , so that the halos within which significant interaction happens may have a broad mass distribution. The number of satellites in a halo, which increases with halo mass, the cold gas reservoir, and the host halo abundance, which decreases with halo mass, working together, may thus make halos with $\log M_{\text{h,A}}/h^{-1}M_{\odot} \sim 12$ the most favorable places for AGN activities.

In Figure 10, we also show the satellite number at different redshifts based on the CSMF of Moster et al. (2010). The satellite number for $\log M_{\text{h,A}}/h^{-1}M_{\odot} = 12$ is close to unity for different redshifts, consistent with the weak redshift dependence of the host halo mass of AGNs (Croom et al. 2005). Since the interaction time scale is expected to be proportional to halo dynamical time, t_{it} is expected to decrease with increasing redshift. Moreover, galaxies at high redshift are expected to contain more cold gas than the low- z counterparts. These two factors together may lead to much stronger and more frequent AGN activities, which may be relevant to quasars observed at high redshift.

One question with this scenario is whether or not small satellites with masses down to $M_{\text{c}}/1000$ are capable of triggering AGN activities. Satellites are usually surrounded by their own dark matter halos (subhalos). For host halos of $\log M_{\text{h}}/h^{-1}M_{\odot} = 12$, $M_{\text{c}} \sim 10^{10.3} h^{-2}M_{\odot}$ according to the SHMR, and so $M_{\text{c}}/1000 \sim 10^{7.3} h^{-2}M_{\odot}$. According to the SHMR for central galaxies, these galaxies reside in halos of $\log M_{\text{h}}/h^{-1}M_{\odot} \sim 10.3$ before becoming satellites. Therefore, halos associated with these satellites may be massive enough to disrupt the interstellar medium in centrals and to induce galactic-scale gas inflow. Since dark halos are more extended than galaxies, they can be severely stripped before interacting with the centrals, the exact mass relevant to the interaction is unclear.

It is also unclear whether or not galactic-scale inflows produced by the interaction with satellite galaxies can directly fuel the central super-massive black holes (SMBHs) to produce AGNs. One possibility is that the galactic-scale inflow can enhance the star formation in a galaxy center to build up a pseudo-bulge/bar component, as indicated by Figure 9, which in turn can help drive cold gas toward the SMBH. Consistent with this, a large fraction of the host galaxies of AGNs are observed to contain pseudo-bulge structures (e.g. Bennert et al. 2015). Alternatively, the interactions with satellites may distort galaxy disks, and the gravitational torque of the non-axisymmetric disks can help to transport cold gas into the galactic center to feed the SMBH (Hopkins & Quataert 2011). These secular structures may persist long after the original interaction, providing a long lasting engine to support AGN activities. Clearly, further investigations are needed to verify such a scenario.

6.4. Halo growth, Interactions, AGN feedback and Galaxy evolution

The efficiency for converting baryonic gas into stars, which can be characterized by $M_{\text{c}}/M_{\text{h}}$, peaks at a mass $\log(M_{\text{h,p}}/h^{-1}M_{\odot}) \sim 12$. Wang et al. (2018a) found that the quenched fraction for centrals increases with M_{h} very quickly around $M_{\text{h,p}}$. These results imply that a large fraction of central galaxies have their star formation quenched

when their halos reach $M_{\text{h,p}}$ (see more discussion on this threshold mass in Dekel & Birnboim 2006; Gabor & Davé 2015). Interestingly, halos of $10^{12} h^{-1}M_{\odot}$ are also important for AGN activities, as shown in Section 4 (see also Croom et al. 2005; Mandelbaum et al. 2009). One scenario proposed in the literature is that AGN feedback can quench the star formation in their host galaxies. This is supported by the high AGN fraction at $D_{\text{n}}4000 = 1.5 \sim 1.6$ (Figure 2), where the transition from star-forming to quiescent population occurs. Since the timescales for AGN activities and quenching are expected to be shorter than that for halo growth, one would expect that AGNs have the same SHMR as star-forming galaxies, consistent with our results in Figure 5. However, there are unresolved problems in this scenario. In the local Universe, AGN radiation and their winds are usually weak (Kauffmann & Heckman 2009), and it may be difficult to expel cold gas from host galaxies. Moreover, the timescale for galaxy quenching is about 1 Gyr, while the timescale for one cycle of AGN activity is much smaller. Thus, the observed AGNs are unlikely the ones that expelled the cold gas and quenched the star formation.

Based on our results, we propose a scenario which is sketched in Figure 11. In this scenario, central galaxies in halos of $\log(M_{\text{h}}/h^{-1}M_{\odot}) < 12$ are mostly star-forming galaxies (see e.g. Wang et al. 2018a), and thus contain large amounts of cold gas. Since the number of satellites per halo in these halos is small, most of the galaxies exhibit no significant AGN activity. When halos grow to about $10^{12} h^{-1}M_{\odot}$, the number of satellites reaches the order of unity, and close interaction happens within a time scale $t_{\text{it}} \sim 3$ Gyrs. Interaction makes the cold gas in the disk flow into the galaxy center, triggering AGN activities and strong star formation (or even a star burst). The AGN associated with the star burst usually has a high accretion rate and luminosity (Kauffmann & Heckman 2009; Greene et al. 2020), and thus can launch strong winds (Wang et al. 2011b) that can quench the star formation in galaxy center and shut off the fuel supply to the AGN. Because of this, the stellar population formed in the star burst evolves from $D_{\text{n}}4000 = 1$ to 1.5 within about 1 Gyr. During this period, secular non-axisymmetric structures produced by the interaction may continue to send cold gas from the disk, albeit at a reduced rate, to feed the SMBH, producing a low-level AGN. In this case, low level AGNs may be triggered multiple times by the secular evolution, so that the total duty cycle time is much longer than that of a single cycle. Since the total amount of cold gas is already reduced by the star burst, the AGNs triggered by the secular evolution are expected to be weak, and no significant enhancement of star formation is expected from the process. As the process proceeds, the host galaxy will become poorer in cold gas, eventually becoming quenched in star formation, and the AGN triggered by the secular structure will become too weak to detect. During this long time scale, halos can still grow significantly while galaxy mass grows little, which may explain why quiescent galaxies have more massive halos than star-forming galaxies of the same stellar mass.

In this scenario, most of the AGNs observed in the local Universe are not associated with star bursts, although their host galaxies may have gone through star burst phases earlier. Indeed, the analyses on the H δ absorption line have revealed that a significant fraction of AGNs reside in post-star-burst galaxies (Kauffmann et al. 2003a). The early star burst in the center of a galaxy can help to build up a central

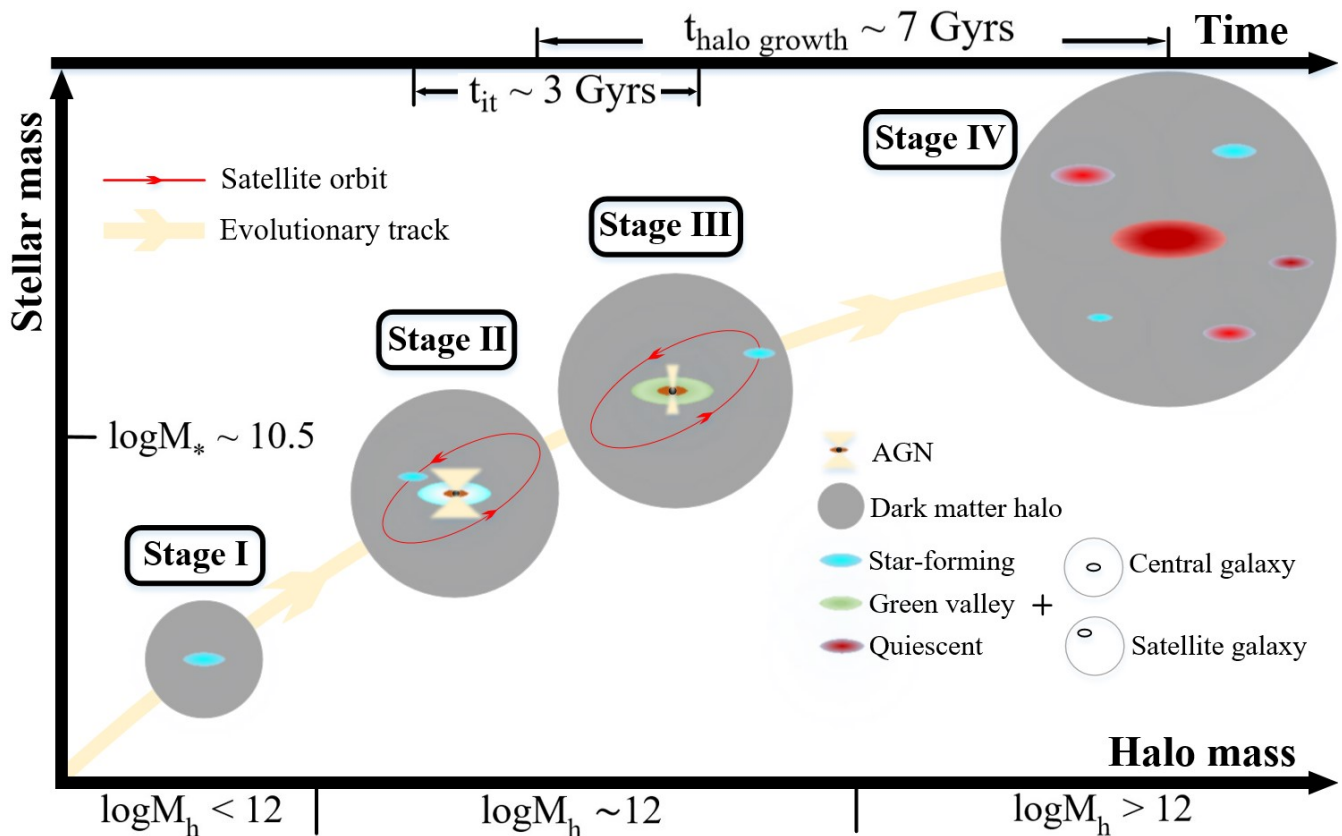


Fig. 11. Sketch of galaxy-halo evolution and AGN triggering through minor interactions. At stage I when halo mass is much less than $10^{12} h^{-1} M_{\odot}$, the halo may only host one central galaxy which contains plenty of cold gas. No significant AGN activity is detected because of the absence of the minor interaction with satellites. At stage II when the halo mass grows to $\sim 10^{12} h^{-1} M_{\odot}$, the number of satellites per halo reaches the order of unity so that interaction between central and satellites may happen within a time scale ~ 3 Gyrs, and consequently makes the cold gas in the disk flow into the galaxy center, triggers AGN activities and strong star formation (or even a star burst). At stage III, star formation in galaxy center has been quenched by star burst and AGN activity and the stellar population formed in the star burst evolves from $D_n 4000 = 1$ to 1.5. The non-axisymmetric structures produced by interaction may continue to drive cold gas inwards, albeit at a reduced rate, producing a low-level AGN multiple times. Since the amount of cold gas is reduced by the star burst, no significant enhancement of star formation is expected during this stage. At stage IV, after a typical timescale of 7 Gyrs, the host halo mass becomes much larger than $10^{12} h^{-1} M_{\odot}$, the star formation in central galaxy is fully quenched owing to the lack of cold gas, and AGN may still be triggered by the secular process but too weak to detect.

bulge. This may explain why galaxies of larger σ_* on average are surrounded by larger number of satellites (Figure 9). The connection between star burst and AGN activity is also supported by the high AGN fraction in galaxies with $D_n 4000 \sim 1$ (Figure 2). Since AGNs in star burst galaxies ($D_n 4000 < 1.2$) are directly triggered by galaxy interaction, while AGNs hosted by galaxies in the transition from star-forming to quiescent populations ($D_n 4000 \sim 1.5$) are mainly driven by secular evolution, two characteristic time scales are relevant here: the star burst time scale, which is typically 10^8 years, and the secular evolution time scale, which is typically a few Gyrs for present-day galaxies. The two peak distribution shown in Figure 2 may be explained by these two time scales.

7. Summary

Based on spectroscopic and shear data of SDSS galaxies in local Universe, we investigate the difference and similarity between optically-selected AGNs and normal galaxies. Here we only focus on the central galaxies of galaxy groups and clusters. We construct control samples for AGNs from

quiescent and star-forming galaxies, respectively, so that we can inspect the location of AGNs in the evolutionary path of galaxies. We investigate the galaxy properties, such as star formation rate, color, $D_n 4000$ and central velocity dispersion, for AGNs and control samples. We use cross-correlation and weak lensing measurements to constrain the halo masses and surrounding satellites of these galaxies. Our main scientific results are summarized as follows.

- The color and $D_n 4000$ distributions for the majority of AGNs are almost independent of the stellar mass (Figure 1). In contrast, star-forming and quiescent galaxies exhibit strong or significant dependence. AGNs have larger (smaller) central velocity dispersion than star-forming (quiescent) galaxies.
- There are two peaks in the distribution of AGN fraction (Figure 2). One peak is at $D_n 4000 \sim 1$ and the other at $D_n 4000 \sim 1.5$. AGN fraction at the first peak strongly depends on stellar mass, ranging from 5% to $>40\%$, while that at the second peak is around 30%, almost independent of stellar mass.
- Combining cross-correlation function and weak lensing signal together, we measure the host halo masses for

AGNs, control star-forming and quiescent galaxies. This technique significantly increases the signal-to-noise ratio for halo mass measurement (Table 1).

- The mean host halo mass for AGNs is around $\log(M_{h,A}/h^{-1}M_{\odot}) = 12$ (Table 1). It is similar to the pivot halo mass in the stellar mass-halo mass relation.
- AGNs and control star-forming galaxies share the same stellar mass-halo mass relation, while quiescent galaxies reside in more massive host halos than the other two populations (Figure 5).
- AGNs are surrounded by more satellites than star-forming galaxies of the same stellar mass (Figure 6 and 7). And the difference is dominated by small satellites with masses down to 10^{-3} of the central stellar mass (Figure 8).
- For galaxies with mass similar to the host galaxies of AGNs, galaxies with larger central velocity dispersion are surrounded by more satellites (Figure 9).
- Control samples have significant impact on the environmental study for AGNs (Figure 6). It is required to take into account the evolutionary stage when constructing control samples.

AGN activities, galaxy quenching and the change of environment (halo mass and satellites) occur at different time scales, ranging from $\ll 0.1$ Gyr to several Gyr. Our results clearly show that, on the timescale for galaxy quenching, optical AGNs look different from normal galaxies. AGNs like to reside in star burst galaxies and ‘green valley’ galaxies that are transiting from star-forming to quiescent phase. However, on a long timescale for halo growth, AGNs are close to star-forming galaxies, but very far from quiescent galaxies in the evolutionary path of galaxies. If the timescale for AGN activities is really very short, less than 0.1 Gyr, as claimed in the literature, multiple AGN activities for one single SMBH are required to explain the high AGN fraction at some specific evolution stages.

We thus propose a scenario, in which minor interactions with small satellites and their dark halos, as well as the warped and unstable galactic structures caused by the interactions, can trigger gas inflow to ignite the AGNs multiple times. The first interaction with satellites can cause strong star formation, even star burst, in galactic center, which may help to buildup the bulges, and trigger AGNs of high luminosity. The feedback from the strong AGNs and star burst ceases the star formation. It can explain various observational facts shown in this paper and previous studies. Interaction probability is dependent on satellite number. We find that the mean number of satellites with $M_s > M_c/1000$ strongly increases with halo mass and reaches about unity around halo mass of $10^{12} h^{-1} M_{\odot}$. Together with the star-forming population and halo abundance quickly declining with halo mass, our scenario provides a natural explanation on why optically selected AGNs favor halos of $10^{12} h^{-1} M_{\odot}$. It may also help to yield the pivot mass in the stellar mass-halo mass relation.

Besides the minor interaction scenario, other processes may also work. For example, major mergers and violent interactions can induce strong gas perturbation and trigger AGN activity. Internal secular evolution forms galactic bars, which cause gas inflow to feed the SMBH. The elliptical shape of halos, which is also correlated with substructure number, can also lead to a non-axisymmetric gravitational potential and cause slow gas inflow. Moreover, the

release of the gravitational energy of these satellites may also help to maintain the circumgalactic gas hot and tenuous. Detailed studies are certainly required to understand the role and efficiency of various mechanisms.

Acknowledgments

We thank the referee for useful comments. This work is supported by the National Key R&D Program of China (grant No. 2018YFA0404503), the National Natural Science Foundation of China (NSFC, Nos. 11733004, 11421303, 11890693, 11522324, 11773032 and 12022306), the National Basic Research Program of China (973 Program) (2015CB857002), and the Fundamental Research Funds for the Central Universities. The work is also supported by the Supercomputer Center of University of Science and Technology of China.

References

- Abazajian, K. N., Adelman-McCarthy, J. K., Agüeros, M. A., et al. 2009, *ApJS*, 182, 543
- Alonso, S., Coldwell, G., Duplancic, F., Mesa, V., & Lambas, D. G. 2018, *A&A*, 618, A149
- Antonucci, R. 1993, *ARA&A*, 31, 473
- Arsenault, R. 1989, *A&A*, 217, 66
- Baldry, I. K., Balogh, M. L., Bower, R. G., et al. 2006, *MNRAS*, 373, 469
- Baldry, I. K., Glazebrook, K., Brinkmann, J., et al. 2004, *ApJ*, 600, 681
- Baldwin, J. A., Phillips, M. M., & Terlevich, R. 1981, *PASP*, 93, 5
- Barro, G., Faber, S. M., Koo, D. C., et al. 2017, *ApJ*, 840, 47
- Barrow, J. D., Bhavsar, S. P., & Sonoda, D. H. 1984, *MNRAS*, 210, 19P
- Behroozi, P., Wechsler, R. H., Hearin, A. P., & Conroy, C. 2019, *MNRAS*, 1134
- Bell, E. F., McIntosh, D. H., Katz, N., & Weinberg, M. D. 2003, *ApJS*, 149, 289
- Bell, E. F., Wolf, C., Meisenheimer, K., et al. 2004, *ApJ*, 608, 752
- Bennert, V. N., Treu, T., Auger, M. W., et al. 2015, *ApJ*, 809, 20
- Bhowmick, A. K., Blecha, L., & Thomas, J. 2020, arXiv e-prints, arXiv:2007.00014
- Bing, L., Shi, Y., Chen, Y., et al. 2019, *MNRAS*, 482, 194
- Blanton, M. R. 2006, *ApJ*, 648, 268
- Blanton, M. R. & Roweis, S. 2007, *AJ*, 133, 734
- Blanton, M. R., Schlegel, D. J., Strauss, M. A., et al. 2005, *AJ*, 129, 2562
- Bluck, A. F. L., Maiolino, R., Sánchez, S. F., et al. 2020, *MNRAS*, 492, 96
- Bluck, A. F. L., Mendel, J. T., Ellison, S. L., et al. 2014, *MNRAS*, 441, 599
- Bluck, A. F. L., Mendel, J. T., Ellison, S. L., et al. 2016, *MNRAS*, 462, 2559
- Brinchmann, J., Charlot, S., White, S. D. M., et al. 2004, *MNRAS*, 351, 1151
- Cacciato, M., van den Bosch, F. C., More, S., et al. 2009, *MNRAS*, 394, 929
- Cappellari, M., Bacon, R., Bureau, M., et al. 2006, *MNRAS*, 366, 1126
- Chown, R., Li, C., Athanassoula, E., et al. 2019, *MNRAS*, 484, 5192
- Conselice, C. J., Chapman, S. C., & Windhorst, R. A. 2003, *ApJ*, 596, L5
- Croom, S. M., Boyle, B. J., Shanks, T., et al. 2005, *MNRAS*, 356, 415
- Croton, D. J., Springel, V., White, S. D. M., et al. 2006, *MNRAS*, 365, 11
- Darg, D. W., Kaviraj, S., Lintott, C. J., et al. 2010, *MNRAS*, 401, 1552
- Dekel, A. & Birnboim, Y. 2006, *MNRAS*, 368, 2
- Delvecchio, I., Lutz, D., Berta, S., et al. 2015, *MNRAS*, 449, 373
- Di Matteo, T., Colberg, J., Springel, V., Hernquist, L., & Sijacki, D. 2008, *ApJ*, 676, 33
- Di Matteo, T., Springel, V., & Hernquist, L. 2005, *Nature*, 433, 604
- Dodd, S. A., Law-Smith, J. A. P., Aucht, K., Ramirez-Ruiz, E., & Foley, R. J. 2020, arXiv e-prints, arXiv:2010.10527

- Ellison, S. L., Patton, D. R., Mendel, J. T., & Scudder, J. M. 2011, *MNRAS*, 418, 2043
- Ellison, S. L., Patton, D. R., Simard, L., & McConnell, A. W. 2008, *AJ*, 135, 1877
- Fabian, A. C. 2012, *ARA&A*, 50, 455
- Fanali, R., Dotti, M., Fiacconi, D., & Haardt, F. 2015, *MNRAS*, 454, 3641
- Foreman-Mackey, D., Hogg, D. W., Lang, D., & Goodman, J. 2013, *PASP*, 125, 306
- Gabor, J. M. & Davé, R. 2015, *MNRAS*, 447, 374
- Gabor, J. M., Impey, C. D., Jahnke, K., et al. 2009, *ApJ*, 691, 705
- Galloway, M. A., Willett, K. W., Fortson, L. F., et al. 2015, *MNRAS*, 448, 3442
- Gao, F., Wang, L., Pearson, W. J., et al. 2020, *A&A*, 637, A94
- Goulding, A. D., Greene, J. E., Bezanson, R., et al. 2018, *PASJ*, 70, S37
- Goulding, A. D., Matthaey, E., Greene, J. E., et al. 2017, *ApJ*, 843, L35
- Greene, J. E., Setton, D., Bezanson, R., et al. 2020, *ApJ*, 899, L9
- Grogin, N. A., Conselice, C. J., Chatzichristou, E., et al. 2005, *ApJ*, 627, L97
- Heckman, T. M. & Best, P. N. 2014, *ARA&A*, 52, 589
- Hong, J., Im, M., Kim, M., & Ho, L. C. 2015, *ApJ*, 804, 34
- Hopkins, P. F., Hernquist, L., Cox, T. J., et al. 2006, *ApJS*, 163, 1
- Hopkins, P. F. & Quataert, E. 2011, *MNRAS*, 415, 1027
- Ilbert, O., McCracken, H. J., Le Fèvre, O., et al. 2013, *A&A*, 556, A55
- Jiang, C. Y., Jing, Y. P., Faltenbacher, A., Lin, W. P., & Li, C. 2008, *ApJ*, 675, 1095
- Jiang, N., Wang, H., Mo, H., et al. 2016, *ApJ*, 832, 111
- Johnston, D. E., Sheldon, E. S., Tasitsiomi, A., et al. 2007, *ApJ*, 656, 27
- Kalfountzou, E., Stevens, J. A., Jarvis, M. J., et al. 2017, *MNRAS*, 471, 28
- Kauffmann, G. & Heckman, T. M. 2009, *MNRAS*, 397, 135
- Kauffmann, G., Heckman, T. M., Tremonti, C., et al. 2003a, *MNRAS*, 346, 1055
- Kauffmann, G., Heckman, T. M., White, S. D. M., et al. 2003b, *MNRAS*, 341, 54
- Khabiboulline, E. T., Steinhardt, C. L., Silverman, J. D., et al. 2014, *ApJ*, 795, 62
- Khim, H. & Yi, S. K. 2017, *ApJ*, 846, 155
- Kocevski, D. D., Brightman, M., Nandra, K., et al. 2015, *ApJ*, 814, 104
- Kormendy, J. & Kennicutt, Robert C., J. 2004, *ARA&A*, 42, 603
- Koss, M., Mushotzky, R., Veilleux, S., & Winter, L. 2010, *ApJ*, 716, L125
- Koulouridis, E., Chavushyan, V., Plionis, M., Krongold, Y., & Dultzin-Hacyan, D. 2006, *The Astrophysical Journal*, 651, 93–100
- Kravtsov, A. V., Vikhlinin, A. A., & Meshcheryakov, A. V. 2018, *Astronomy Letters*, 44, 8
- Kroupa, P. 2001, *MNRAS*, 322, 231
- Lackner, C. N., Silverman, J. D., Salvato, M., et al. 2014, *AJ*, 148, 137
- Laurent, P., Eftekharzadeh, S., Le Goff, J.-M., et al. 2017, *J. Cosmology Astropart. Phys.*, 2017, 017
- Leauthaud, A., Tinker, J., Bundy, K., et al. 2012, *ApJ*, 744, 159
- Lewis, A. & Challinor, A. 2011, *CAMB: Code for Anisotropies in the Microwave Background*
- Li, C., Kauffmann, G., Heckman, T. M., White, S. D. M., & Jing, Y. P. 2008, *MNRAS*, 385, 1915
- Li, C., Kauffmann, G., Jing, Y. P., et al. 2006a, *MNRAS*, 368, 21
- Li, C., Kauffmann, G., Wang, L., et al. 2006b, *MNRAS*, 373, 457
- Li, P., Wang, H., Mo, H. J., Wang, E., & Hong, H. 2020, *ApJ*, 902, 75
- Li, Y. 2019, *mcfit: Multiplicatively Convolutional Fast Integral Transforms*
- Luo, W., Yang, X., Lu, T., et al. 2018, *ApJ*, 862, 4
- Luo, W., Yang, X., Zhang, J., et al. 2017, *ApJ*, 836, 38
- Mahoro, A., Pović, M., & Nkundabakura, P. 2017, *MNRAS*, 471, 3226
- Man, Z.-y., Peng, Y.-j., Kong, X., et al. 2019, *MNRAS*, 488, 89
- Mandelbaum, R., Hirata, C. M., Seljak, U., et al. 2005, *MNRAS*, 361, 1287
- Mandelbaum, R., Li, C., Kauffmann, G., & White, S. D. M. 2009, *MNRAS*, 393, 377
- Mandelbaum, R., Seljak, U., Kauffmann, G., Hirata, C. M., & Brinkmann, J. 2006, *MNRAS*, 368, 715
- Marconi, A., Risaliti, G., Gilli, R., et al. 2004, *MNRAS*, 351, 169
- Miralda-Escude, J. 1991, *ApJ*, 370, 1
- Mo, H. J. & White, S. D. M. 1996, *MNRAS*, 282, 347
- Moore, B., Katz, N., Lake, G., Dressler, A., & Oemler, A. 1996, *Nature*, 379, 613
- Moster, B. P., Somerville, R. S., Maulbetsch, C., et al. 2010, *ApJ*, 710, 903
- Mulchaey, J. S. & Regan, M. W. 1997, *ApJ*, 482, L135
- Mullaney, J. R., Alexander, D. M., Aird, J., et al. 2015, *MNRAS*, 453, L83
- Muzzin, A., Marchesini, D., Stefanon, M., et al. 2013, *ApJ*, 777, 18
- Navarro, J. F., Frenk, C. S., & White, S. D. M. 1997, *ApJ*, 490, 493
- Oh, S., Oh, K., & Yi, S. K. 2012, *ApJS*, 198, 4
- Pasquali, A., van den Bosch, F. C., Mo, H. J., Yang, X., & Somerville, R. 2009, *MNRAS*, 394, 38
- Peng, Y.-j., Lilly, S. J., Kovač, K., et al. 2010, *ApJ*, 721, 193
- Pierce, C. M., Lotz, J. M., Laird, E. S., et al. 2007, *ApJ*, 660, L19
- Powell, M. C., Cappelluti, N., Urry, C. M., et al. 2018, *ApJ*, 858, 110
- Reddick, R. M., Wechsler, R. H., Tinker, J. L., & Behroozi, P. S. 2013, *ApJ*, 771, 30
- Rodighiero, G., Brusa, M., Daddi, E., et al. 2015, *ApJ*, 800, L10
- Sabater, J., Best, P. N., & Argudo-Fernández, M. 2013, *MNRAS*, 430, 638
- Satyapal, S., Ellison, S. L., McAlpine, W., et al. 2014, *MNRAS*, 441, 1297
- Schawinski, K., Koss, M., Berney, S., & Sartori, L. F. 2015, *MNRAS*, 451, 2517
- Sellwood, J. A. 2014, *Reviews of Modern Physics*, 86, 1
- Shankar, F., Allevalo, V., Bernardi, M., et al. 2019, *arXiv e-prints*, arXiv:1910.10175
- Sheldon, E. S., Johnston, D. E., Frieman, J. A., et al. 2004, *AJ*, 127, 2544
- Shen, Y., McBride, C. K., White, M., et al. 2013, *ApJ*, 778, 98
- Silk, J. & Rees, M. J. 1998, *A&A*, 331, L1
- Simpson, C. 2005, *MNRAS*, 360, 565
- Strateva, I., Ivezić, Ž., Knapp, G. R., et al. 2001, *AJ*, 122, 1861
- Tinker, J. L., Robertson, B. E., Kravtsov, A. V., et al. 2010, *ApJ*, 724, 878
- Tomczak, A. R., Quadri, R. F., Tran, K.-V. H., et al. 2014, *ApJ*, 783, 85
- van den Bosch, F. C., Aquino, D., Yang, X., et al. 2008, *MNRAS*, 387, 79
- Viola, M., Cacciato, M., Brouwer, M., et al. 2015, *MNRAS*, 452, 3529
- Wang, E., Wang, H., Mo, H., et al. 2018a, *ApJ*, 860, 102
- Wang, H., Mo, H. J., Chen, S., et al. 2018b, *ApJ*, 852, 31
- Wang, H., Mo, H. J., Jing, Y. P., Yang, X., & Wang, Y. 2011a, *MNRAS*, 413, 1973
- Wang, H., Mo, H. J., Yang, X., et al. 2016, *ApJ*, 831, 164
- Wang, H., Wang, T., Zhou, H., et al. 2011b, *ApJ*, 738, 85
- Wang, L. & Li, C. 2019, *MNRAS*, 483, 1452
- Wechsler, R. H. & Tinker, J. L. 2018, *ARA&A*, 56, 435
- Weinmann, S. M., van den Bosch, F. C., Yang, X., & Mo, H. J. 2006, *MNRAS*, 366, 2
- Wetzel, A. R., Tinker, J. L., & Conroy, C. 2012, *MNRAS*, 424, 232
- Woo, J., Dekel, A., Faber, S. M., et al. 2013, *MNRAS*, 428, 3306
- Yang, X., Mo, H. J., & van den Bosch, F. C. 2003, *MNRAS*, 339, 1057
- Yang, X., Mo, H. J., & van den Bosch, F. C. 2009, *ApJ*, 695, 900
- Yang, X., Mo, H. J., van den Bosch, F. C., & Jing, Y. P. 2005, *MNRAS*, 356, 1293
- Yang, X., Mo, H. J., van den Bosch, F. C., et al. 2006, *MNRAS*, 373, 1159
- Yang, X., Mo, H. J., van den Bosch, F. C., et al. 2007, *ApJ*, 671, 153
- Yuan, F., Yoon, D., Li, Y.-P., et al. 2018, *ApJ*, 857, 121
- Zhang, S., Wang, T., Wang, H., & Zhou, H. 2013, *ApJ*, 773, 175